

AD-A152130

RIA-85-U8

AD A152130

TECHNICAL REPORT ARLCB-TR-85001

**ELECTRICAL RESISTIVITY IN AMORPHOUS METALS :
CONSEQUENCES OF PHONON INEFFECTIVENESS
IN THE DIFFRACTION MODEL**

L. V. MEISEL

P.J. COTE

PROPERTY OF
TECHNICAL LIBRARY
ROCK ISLAND ARSENAL
ROCK ISLAND, IL 61229

JANUARY 1985



**US ARMY ARMAMENT RESEARCH AND DEVELOPMENT CENTER
LARGE CALIBER WEAPON SYSTEMS LABORATORY
BENÉT WEAPONS LABORATORY
WATERVLIET N.Y. 12189**

APPROVED FOR PUBLIC RELEASE; DISTRIBUTION UNLIMITED

DISCLAIMER

The findings in this report are not to be construed as an official Department of the Army position unless so designated by other authorized documents.

The use of trade name(s) and/or manufacture(s) does not constitute an official indorsement or approval.

DISPOSITION

Destroy this report when it is no longer needed. Do not return it to the originator.

REPORT DOCUMENTATION PAGE		READ INSTRUCTIONS BEFORE COMPLETING FORM
1. REPORT NUMBER ARLCB-TR-85001	2. GOVT ACCESSION NO.	3. RECIPIENT'S CATALOG NUMBER
4. TITLE (and Subtitle) ELECTRICAL RESISTIVITY IN AMORPHOUS METALS: CONSEQUENCES OF PHONON INEFFECTIVENESS IN THE DIFFRACTION MODEL		5. TYPE OF REPORT & PERIOD COVERED Final
		6. PERFORMING ORG. REPORT NUMBER
7. AUTHOR(s) L. V. Meisel and P. J. Cote		8. CONTRACT OR GRANT NUMBER(s)
9. PERFORMING ORGANIZATION NAME AND ADDRESS US Army Armament Research & Development Center Benet Weapons Laboratory, SMCAR-LCB-TL Watervliet, NY 12189-5000		10. PROGRAM ELEMENT, PROJECT, TASK AREA & WORK UNIT NUMBERS AMCMS NO. 6111.02.H600.011 PRON NO. 1A325B541A1A
11. CONTROLLING OFFICE NAME AND ADDRESS US Army Armament Research & Development Center Large Caliber Weapon Systems Laboratory Dover, NJ 07801-5001		12. REPORT DATE January 1985
		13. NUMBER OF PAGES 47
14. MONITORING AGENCY NAME & ADDRESS (if different from Controlling Office)		15. SECURITY CLASS. (of this report) Unclassified
		15a. DECLASSIFICATION/DOWNGRADING SCHEDULE
16. DISTRIBUTION STATEMENT (of this Report) Approved for Public Release; Distribution Unlimited		
17. DISTRIBUTION STATEMENT (of the abstract entered in Block 20, if different from Report)		
18. SUPPLEMENTARY NOTES Published in Physical Review B Journal.		
19. KEY WORDS (Continue on reverse side if necessary and identify by block number) Amorphous Metals Electron-Phonon Interaction Electrical Transport		
20. ABSTRACT (Continue on reverse side if necessary and identify by block number) Electrical transport in amorphous metals is analyzed in the context of the Baym-Faber-Ziman theory. The theory is generalized to incorporate electron mean free path effects through the Pippard-Ziman condition on the electron-phonon interaction. A variety of model t-matrices are considered. The geometrical structure factors are modeled by Percus-Yevick hard sphere forms and a single branch Debye phonon spectrum is assumed. Detailed results for electrical (CONT'D ON REVERSE)		

20. ABSTRACT (CONT'D)

resistivity ρ vs. temperature T and the TCR are presented for extensive ranges of $2k_F/k_p$ and electron mean free path. The results, incorporating the Pippard-Ziman condition, are consistent with the observed ρ vs. T in low resistivity glassy metals. However, although inclusion of the Pippard-Ziman condition dramatically improves agreement with the data, quantitative agreement is not obtained in high resistivity amorphous metals.

TABLE OF CONTENTS

	<u>Page</u>
INTRODUCTION	1
THEORY	6
MODELS AND COMPUTATIONAL DETAILS	7
RESULTS	11
Substitutional Models	11
Effective Potential Models	16
DISCUSSION	17
CONCLUSIONS	24
REFERENCES	26

LIST OF ILLUSTRATIONS

1. Normalized resistivity difference (Eq. (19)) for the $ t_1 - t_2 ^2$ term in Eq. (12b) versus normalized temperature (Eq. (16)) for the constant t-matrix substitutional model. The curves in Figures 1 through 7 parameterized A, B, C, D, E, and F designate results for $q\eta\Lambda = 300, 18, 12, 6, 4,$ and $2,$ respectively.	29
2. Normalized temperature coefficient of resistivity (Eq. (17)) for the averaged t-matrix term (i.e., the $ c_1 t_1 + c_2 t_2 ^2$ term) in Eq. (12b) versus $2k_F/k_p$ for the constant t-matrix substitutional model. (Parameters as in Figure 1.)	30
3. Normalized resistivity difference (Eq. (18)) for the averaged t-matrix term in Eq. (12b) versus normalized temperature (Eq. (16)) for the constant t-matrix substitutional model for $2k_F = 0.9 k_p$. (Parameters as in Figure 1.)	31
4a. Normalized resistivity difference versus normalized temperature as in Figure 3 for $2k_F = 1.05 k_p$.	32
4b. Normalized resistivity difference versus normalized temperature as in Figure 3 for $2k_F = 1.05 k_p$.	33
5a. Normalized resistivity difference versus normalized temperature as in Figure 3 for $2k_F = 1.15 k_p$.	34

	<u>Page</u>
5b. Normalized resistivity difference versus normalized temperature as in Figure 3 for $2k_F = 1.15 k_p$.	35
6a. Normalized resistivity difference versus normalized temperature as in Figure 3 for $2k_F = 1.30 k_p$.	36
6b. Normalized resistivity difference versus normalized temperature as in Figure 3 for $2k_F = 1.30 k_p$.	37
7a. Normalized resistivity difference versus normalized temperature as in Figure 3 for $2k_F = 1.40 k_p$.	38
7b. Normalized resistivity difference versus normalized temperature as in Figure 3 for $2k_F = 1.40 k_p$.	39
8a. Normalized resistivity difference versus normalized temperature as in Figure 3 for $q_D\Lambda = 12$. The parameters are $2k_F/k_p$ values. Parts (a) and (b) are from the left and right of $2k_F/k_p$ corresponding to the largest negative tcr.	40
8b. Normalized resistivity difference versus normalized temperature as in Figure 3 for $q_D\Lambda = 12$. The parameters are $2k_F/k_p$ values. Parts (a) and (b) are from the left and right of $2k_F/k_p$ corresponding to the largest negative tcr.	41
9. Normalized resistivity difference versus normalized temperature as in Figure 3 for $q_D\Lambda = 6$. The parameters are $2k_F/k_p$ values.	42
10. Normalized temperature coefficient of resistivity (Eq. (17)) versus $2k_F/k_p$ for the a-Mg ₇ Zn ₃ substitutional model. The parameters are $q_D\Lambda$ values.	43
11. Normalized resistivity difference (ρ substituted for r in Eq. (18) versus normalized temperature for the a-Mg ₇ Zn ₃ substitutional model with $q_D\Lambda = 12$. The parameters are $2k_F/k_p$ values. (N.b. Normalization is with respect to ρ at $\tau = 0.01$ rather than $\tau = 0$ in this and the next figure only.)	44
12. Normalized resistivity difference versus normalized temperature for the potassium pseudoatom effective potential model with $q_D\Lambda = 12$. The parameters are $2k_F/k_p$ values.	45

INTRODUCTION

The electrical resistivity ρ of amorphous metals is usually described in the context of the diffraction model, i.e., in terms of the Baym-Faber-Ziman (refs 1-3) theory. The temperature T dependence of $\rho(T)$ is essentially determined by that of the resistivity static structure factor (refs 4,5) $S^\rho(K)$ where \vec{K} is the scattering vector. The resistivity is actually given by a weighted average of the product of $S^\rho(K)$ and the absolute square of the scattering matrix element or t-matrix (ref 6) $t(K)$ which is independent of T . (It is to be understood that references to $a(K)$, $S^\rho(K)$, and $t(K)$ are to be generalized to the appropriate partial structure factors and constituent t-matrices in alloys.)

For transition metals, it is often assumed that backscattering (i.e., $K \approx 2k_F$, where k_F is the Fermi wavenumber) is dominant (ref 7). In such cases one has

$$\rho(T)/\rho(\theta) \approx S_T^\rho(2k_F)/S_\theta^\rho(2k_F) \quad (1)$$

where the T dependence of the resistivity static structure factor is explicitly indicated and θ is the Debye temperature. The geometrical structure factor

$$a(K) = \frac{1}{N} \sum_{\vec{m}, \vec{n}} \exp(i\vec{K} \cdot (\vec{m} - \vec{n})) \quad (2)$$

where \vec{m} is the averaged position vector for the m^{th} ion plays the central role in determining $S^\rho(K)$ and hence $\rho(T)$. The scattering vector corresponding to the first peak in $a(K)$ is denoted k_p and the ratio of $2k_F/k_p$ is prominent in the diffraction model description of electrical transport in amorphous alloys.

References are listed at the end of this report.

To apply the diffraction model in the general case (not restricted to the backscattering dominant approximation of Eq. (1)), one requires expressions for $S^p(K)$ and $|t(K)|^2$ for $0 < K < 2k_F$. $S^p(K)$ has been computed (refs 5,8) for Debye phonon spectra and for model $a(K)$ although in principle one could employ a more realistic phonon spectrum and measured $a(K)$. This is done for reasons of simplicity and because $a(K)$ can be nicely approximated by analytic Percus-Yevick hard sphere forms (ref 9) for K in the region of the first peak and because the details of the phonon spectrum are believed to be unimportant in determining $S^p(K)$. The t -matrix is usually approximated by tabulated pseudopotential forms or in terms of expressions involving scattering phase shifts (ref 7) $\eta_\ell(E_F)$ evaluated at the Fermi energy E_F for angular momentum quantum number ℓ . The pseudopotential applications in liquids (refs 2,10) agreed reasonably well with experiment although there were indications that Born approximation was inadequate even for column I and II metals (ref 11). The t -matrix forms, which incorporate single site multiple scattering, are believed to be necessary for the treatment of most glassy metals.

Many of the predictions of the diffraction model for electrical transport in amorphous metals are approximately independent of $t(K)$. Some of the results (ref 8) include:

(i) The concentration dependence of ρ is determined (essentially) by $a(2k_F)$, which can be approximated by simple functions of $2k_F/k_p$. (The concentration dependence of k_F is assumed to be known and k_p is often assumed to be fixed in this prescription.)

(ii) The temperature coefficient of resistivity at the Debye temperature TCR is defined as

$$\text{TCR} \equiv \partial \ln \rho / \partial T|_{T=\theta} \quad (3)$$

The diffraction model, in the "dominant backscattering" approximation yields

$$\text{TCR} \approx \partial \ln[S^{\rho}(2k_F)] / \partial T|_{T=\theta} \quad (3')$$

Results based on Eq. (3') are independent of the actual constituents of the alloys and have the appealing attribute of depending solely on $2k_F/k_p$ and the atomic arrangement. For typical amorphous metals negative TCR is predicted (ref 8) for $0.9 \lesssim 2k_F/k_p \lesssim 1.1$. (This range of $2k_F/k_p$ is broader than that seen in liquid metals.) The magnitude and sign of the TCR may be expressed in terms of the Debye-Waller exponent $2W(2k_F)$, evaluated at $T = \theta$ and $K = 2k_F$, the averaged resistivity structure factor $A_T^{\rho}(K)$, and the Debye integral I_2 , defined in Reference 5.

(iii) At low temperatures, the $S^{\rho}(K)$ and hence the normal state resistivity varies like $[1 + (\pi^2/6)\alpha(T/\theta)^2]$ independent of the sign of the TCR as defined in Eq. (3). The constant α , which also appears in the standard expression for the Debye-Waller exponent, is given by

$$\alpha \equiv 12 \hbar^2 k_F^2 / M k_B \theta \quad (4)$$

for a Debye phonon spectrum where \hbar is Plank's constant divided by 2π , M is the averaged ionic mass, and k_B is Boltzmann's constant.

(iv) Small maxima in $S^{\rho}(K)$ are predicted in negative TCR cases. We denote the temperature corresponding to the maximum in S^{ρ} by T_M . The theory then yields the result that both T_M and $S_{T_M}^{\rho}(2k_F)/S_{0^\circ K}^{\rho}(2k_F) - 1.0$ and thus $\rho(T_M)/\rho(0^\circ K) - 1.0$ decrease as $2k_F$ approaches k_p from either side.

The success of the diffraction model in describing electrical transport in amorphous metals has been mixed. The concentration dependence of the magnitude of ρ is apparently well described. However, only qualitative

agreement with the T dependence has been obtained in low ρ alloys (refs 12-14) and serious disagreements are seen in high ρ alloys (refs 15-17). Some of the discrepancies between the theoretical predictions and the data include: (i) A considerably larger range of $2k_F/k_p$ than predicted yields negative TCR. (ii) The observed negative TCR's are generally larger than predicted (unless unreasonably small θ values are assumed). (iii) The quadratically increasing resistivity at lowest T is often not observed. High resistivity alloys even exhibit monotonic decreasing ρ vs. T in most cases.

The inconsistency of theory and experiment in the high ρ (i.e., $\rho > 100 \mu\Omega\text{cm}$) cases has been viewed as an example of Mooij phenomena (ref 16) or saturation effects (ref 18). Meisel and Cote (ref 15) and Morton et al (ref 19) formulated a generalization of the theory by incorporating the Pippard-Ziman condition (ref 20,21) on the electron-phonon interaction. The condition as stated by Ziman (ref 20) takes the form: "Phonons whose wavelengths $2\pi/q$ exceed the electron mean free path Λ are ineffective electron scatterers". The concept had originally been applied to describe ultrasonic attenuation (ref 21) and was subsequently also shown to be relevant to thermal conductivity (ref 22) and degradation of superconducting transition temperature (ref 23) in high resistivity alloys. Incorporating this constraint into the diffraction model yielded improved agreement with experiment in high resistivity metals.

Recently, low resistivity ($\rho < 100 \mu\Omega\text{cm}$) amorphous non-transition metal alloys were the subjects of detailed experimental study by Mizutani and coworkers (ref 13). Determinations of $\rho(T)$ for $4 \text{ K} \lesssim T \lesssim 300 \text{ K}$, k_F , and k_p were made. It had been expected that the diffraction model unadorned with

saturation effects would give a good description of electrical transport in such alloys because of the relatively long electron mean free path Λ . Thus, calculations were performed for a-MgZn (ref 12). An effective scattering matrix element (i.e., t-matrix), was constructed to yield the observed magnitude of ρ , to have s and p character only, and to satisfy the Friedel sum rule. The geometrical structure factor was assumed to be of Percus-Yevick hard sphere form with $\eta = 0.525$. The result of this calculation was in qualitative agreement with the data (ref 13). However, when phonon ineffectiveness effects with appropriate electron mean free path was incorporated, remarkable agreement was obtained, including such features as: (i) the magnitude of the TCR; (ii) the magnitude and position of the maximum in $\rho(T)/\rho(0)$; (iii) the shape and extent of the approximate $(T-T_M)^{3/2}$ region to the right of T_M ; (iv) the shape and extent of the quadratic in T region; and (v) the position and magnitude of the minimum in $\rho(T)$ observed near 5 K.

Calculations were also performed for four other values of $2k_F/k_p$ employing the a-MgZn effective t-matrix and electron mean free path. These results were used as a basis for discussing electrical transport in general low resistivity alloys. A principal conclusion in that study was that a procedure incorporating phonon ineffectiveness into the diffraction model (as had been suggested for high resistivity amorphous metals (ref 15)) yields much better results, especially in regard to low temperature "anomalies" in $\rho(T)$ and the magnitude of the TCR.

The results of Reference 12 suggested that further detailed investigation of the implications of the diffraction model, incorporating the Pippard-Ziman condition on the electron-phonon interaction, were justified. We have begun a

program of such studies. Initial results were presented at the LAM 5 conference (ref 24). The present paper extends the range of $q_D \Lambda$ investigated to considerably smaller values (corresponding to $\rho > 150 \mu\Omega\text{cm}$) and presents $\rho(T)$ results on a denser $2k_F/k_D$ grid and a broader selection of model t -matrices is employed. The theoretical $\rho(T)$ curves provide a basis for the interpretation of the low T behaviors seen in amorphous metals (especially non-magnetic alloys) and for the observed magnitudes of the TCR.

Reviews of the theoretical concepts described here and summaries of the experimental data are given in References 25 through 27.

THEORY

The Baym-Ziman-Faber (refs 1-3) expression for the electrical resistivity is

$$\rho = B \int_0^1 d\left(\frac{K}{2k_F}\right) \left(\frac{K}{2k_F}\right)^3 |U(K)|^2 \quad (5)$$

where $B = 12 \pi \Omega_0 / e^2 \hbar V_F^2$, Ω_0 is the atomic volume, V_F is the Fermi velocity, e is the electron charge, and

$$\begin{aligned} |U(K)|^2 = & \sum_{ij} c_i c_j S_{ij}^\rho(K) t_i^*(K) t_j(K) \\ & + \left\{ \sum_i c_i |t_i(K)|^2 - \sum_{ij} c_i c_j t_i^*(K) t_j(K) \right\} I^\rho(K) \end{aligned} \quad (6)$$

where c_i is the concentration of the i^{th} constituent and in Sham-Ziman approximation (ref 28), incorporating the Pippard-Ziman condition (ref 20), and for a Debye phonon spectrum, the partial resistivity structure factors are given by

$$S_{ij}^{\rho}(K) = e^{-2W(K)} a_{ij}(K) + \alpha \frac{\Theta}{T} \left(\frac{K}{2k_F}\right)^2 \int_0^1 d\left(\frac{q}{q_D}\right) \left(\frac{q}{q_D}\right)^2 n(x) [n(x) + 1] F(q\Lambda) \int \frac{dq}{4\pi} a_{ij}(\vec{K}+\vec{q}) \quad (7)$$

and

$$I^{\rho}(K) = e^{-2W(K)} + \alpha \frac{\Theta}{T} \left(\frac{K}{2k_F}\right)^2 \int d\left(\frac{q}{q_D}\right) \left(\frac{q}{q_D}\right)^2 n(x) [n(x) + 1] F(q\Lambda) \quad (8)$$

where $x = \frac{\hbar\omega}{k_B T} = \frac{\Theta}{T} \frac{q}{q_D}$, $n(x) = (e^x - 1)^{-1}$, and $F(q\Lambda)$ expresses the reduction

in electron-phonon interaction for small $q\Lambda$ (where q is the phonon wavenumber and Λ the electron mean free path). We employ the Pippard form (ref 21) in the calculations presented here, i.e.,

$$F(y) = \frac{2}{\pi} \left[\frac{y \tan^{-1} y}{y - \tan^{-1} y} - \frac{3}{y} \right] \quad (9)$$

The scattering matrix element (t-matrix) of the j^{th} constituent is expressed in terms of scattering phase shifts $\eta_{\ell}^j(E_F)$ evaluated at the Fermi energy E_F for angular momentum quantum number ℓ as

$$t_j(K) = \frac{2\pi\hbar^3}{m(2mE_F)^{1/2}\Omega_0} \sum_{\ell} (2\ell+1) \sin \eta_{\ell}^j(E_F) e^{i\eta_{\ell}^j(E_F)} P_{\ell}(\cos \theta) \quad (10)$$

where m is the electron mass, $P_{\ell}(x)$ is the ℓ^{th} Legendre polynomial, and $\cos \theta = 1 - 2(K/2k_F)^2$. These equations are generalizations (refs 15,19,25) of those usually employed in liquid and amorphous metal electrical transport studies.

MODELS AND COMPUTATIONAL DETAILS

We do not present results for general alloy systems. Two types of models, which we refer to as the "binary substitutional model" and the

"effective potential models" are discussed. We define them as follows.

A. Binary substitutional models. We refer to systems which satisfy

$$a_{ij}(K) \approx a(K) \text{ for all } i, j \quad (11)$$

as "substitutional", since Eq. (11) will be obtained if the alloy constituents are randomly substituted for each other on a given network of sites. For binary systems satisfying this condition, Eq. (16) reduces to

$$|U(K)|^2 = c_1 c_2 |t_1(K) - t_2(K)|^2 I^{\rho}(K) + |c_1 t_1(K) + c_2 t_2(K)|^2 S^{\rho}(K) \quad (6)$$

We have obtained results for two cases:

A1. Constant t-matrix (pure s-wave scattering). Equation (5) reduces to

$$\rho = B \{ c_1 c_2 \Delta^2 \int_0^1 dx x^3 I^{\rho}(2k_F x) + |\bar{t}|^2 \int_0^1 dx x^3 S^{\rho}(2k_F x) \} \quad (12a)$$

$$\equiv c_1 c_2 B \Delta^2 r_D(q_D \Lambda, T/\Theta) + B |\bar{t}|^2 r(q_D \Lambda, 2k_F/k_p, T/\Theta) \quad (12b)$$

One can conceive of an extensive class of t-matrices for which Eq. (12a) would be approximately valid; Δ and \bar{t} would be averages of the actual linear combinations of t-matrices; for example,

$$\Delta = |t_1(2k_F) - t_2(2k_F)|$$

and

$$\bar{t} = c_1 t_1(2k_F) + c_2 t_2(2k_F)$$

might produce useful approximate expressions for the discussion of $\rho(q_D \Lambda, 2k_F/k_p, T/\Theta)$.

A2. Generalized a-Mg_{1-x}Zn_x for x = 0.225. The t-matrices in this model, representing Mg and Zn, were employed in the calculations presented at LAM5 (ref 24). The t-matrices were computed by the Slater X_α-Method (ref 28) with Herman and Skillman (ref 29) neutral atom wave functions and free electron E_F employing computer routines based on those given by Loucks (ref 30). The Kmetko (ref 31) value of X_α (viz. 0.75) was taken for Mg and X_α = 0.85 was

chosen for Zn in order to place the d-bands in accord with photoemission data (ref 32). The resulting phase shifts were $\eta_{\ell}^{\text{Zn}}(E_F) = 0.354, 0.294, -0.057, \text{ and } 0.002$ and $\eta_{\ell}^{\text{Mg}}(E_F) = -0.175, 0.085, 0.034, \text{ and } 0.001$ for $\ell = 0$ to 3, respectively. The $\eta_{\ell}(E_F)$ for $\ell > 3$ were set to 0. (The results obtained for this potential will be seen to be well approximated by the constant t-matrix results with $|\bar{t}|^2 \gg c_1 c_2 \Delta^2$.)

B. Effective potential model. When the scattering t-matrices are all equal, i.e.,

$$t_i(K) = t_E(K) \text{ for all } i \quad (13)$$

then

$$|U_E(K)|^2 = S_E^{\rho}(K) |t_E(K)|^2 \quad (14)$$

where

$$S_E^{\rho}(K) \equiv \sum c_i c_j S_{ij}^{\rho}(K) \quad (15)$$

One refers to $t_E(K)$ as the effective t-matrix and $S_E^{\rho}(K)$ as the effective resistivity static structure factor. The effective potential results discussed in this report assume that S_E^{ρ} can be computed according to the usual prescriptions with $a_E(K)$ again a Percus-Yevick hard sphere form with $\eta = 0.525$. Thus, these effective potential results are identical with substitutional model results when $t_1(K) = t_2(2)$. One might expect Eq. (13) would be a good approximation if the t-matrices are pseudopotential forms (because they are generally very similar), or if the constituents come from the same column of the periodic chart (e.g., a-MgZn). We have performed effective potential calculations for t-matrices (i) computed for Zn as described in the generalized a-Mg_{0.775}Zn_{0.225} model, (ii) an s and p based form described in Reference 12, and (iii) the pseudopotential based forms given by Young, Meyer, and Kilby (ref 11) particularly for potassium.

We introduce the following normalized variables:

$$\tau \equiv T/\theta \quad (16)$$

$$tcr \equiv (\theta/\alpha)TCR \equiv (1/\alpha) \partial \ln \rho / \partial \tau |_{\tau=1} \quad (17)$$

$$R(q_D \Lambda, \frac{2k_F}{k_p}, \tau) \equiv \frac{1}{\alpha} \left[\frac{r(q_D \Lambda, 2k_F/k_p, \tau)}{r(q_D \Lambda, 2k_F/k_p, 0)} - 1 \right] \quad (18)$$

and

$$R_D(q_D \Lambda, \tau) \equiv \frac{1}{\alpha} \left[\frac{r_D(q_D \Lambda, \tau)}{r_D(q_D \Lambda, 0)} - 1 \right] \quad (19)$$

We refer to R or R_D as normalized resistivity differences. We shall also denote by tcr the result of replacing ρ by $r(q_D \Lambda, 2k_F/k_p, \tau)$ or $r_D(q_D \Lambda, \tau)$ in Eq. (17). The tcr , R and R_D , are approximately independent of α . (We shall also use Eq. (18) to define a normalized R when ρ is substituted for r on the right-hand side.)

Thus, in the constant t -matrix substitutional model (A1), one has:

$$\rho(\tau) = \rho(0)[1 + \alpha(K_D R_D(\tau) + K R(\tau))] \quad (20)$$

and

$$\frac{1}{\alpha} \frac{\partial \ln \rho}{\partial \tau} \Big|_{\tau=1} \approx K_D \cdot tcr_D + K \cdot tcr \quad (21)$$

where

$$K \equiv |\bar{t}|^2 r(0) / (|\bar{t}|^2 r(0) + c_1 c_2 \Delta^2 r_D(0)) \quad (22)$$

and

$$K_D \equiv 1 - K \quad (23)$$

We have suppressed the $q_D \Lambda$ and $2k_F/k_p$ parameters in these equations and tcr and tcr_D are deduced from $r(\tau)$ and $r_D(\tau)$, respectively. Equation (21) is approximate because we have neglected $\alpha R_D(1)$ and $\alpha R(1)$ with respect to unity.

RESULTS

Substitutional Models

Model A1. Constant t-matrix substitutional model.

Most of the results presented in this report are computed for this model. The value of α was fixed at 0.168, but the "normalized" results do not depend strongly on α . We also assumed $q_D = k_F$ in all calculations. Thus, when considering an alloy series one might have to allow for the possibility that q_D might be essentially constant while k_F varies with concentration. The geometrical structure factors were modeled by Percus-Yevick forms with $\eta = 0.525$ and include the $N\delta_{K,0}$ term.

Figure 1 shows plots of $R_D(q_D\Lambda, \tau)$ vs. τ for $q_D\Lambda = 2, 4, 6, 12, 18, 300$. Notice that: (i) Although for $\tau \gg 1$ the $R_D(300, \tau)$ curve is essentially flat, $R_D(300, \tau)$ still has a relatively large positive slope near $\tau = 1$. (ii) $R_D(18, \tau)$ is essentially flat near $\tau = 1$. (iii) For $q_D\Lambda < 18$, all $R_D(q_D\Lambda, \tau)$ have negative slope near $\tau = 1$. (iv) $R_D(12, \tau)$ exhibits a broad (relatively) large maximum near $\tau = 0.5$. (We shall denote the value of τ corresponding to maxima as τ_M . Hence $\tau_M \approx 0.5$.) (v) At $q_D\Lambda = 6$, $\tau_M \approx 0.3$. (vi) There are usually small minima in the curves which exhibit maxima. We denote the normalized temperature corresponding to a minimum by τ_m . Hence $\tau_m \approx 0.04$ and 0.08 for $q_D\Lambda = 12$ and 6 , respectively. (vii) As $q_D\Lambda$ decreases, τ_M decreases and τ_m increases until a critical value $(q_D\Lambda)_c$ is reached where the minimum and maximum coalesce and for $q_D\Lambda < (q_D\Lambda)_c$ monotonic decreasing behavior is observed. For $q_D\Lambda \lesssim (q_D\Lambda)_c$ the curves show a "knee". At $q_D\Lambda = 4$ a knee occurs near $\tau = 0.2$, so it appears that $(q_D\Lambda)_c \approx 4$. (viii) $R_D(2, \tau)$ decreases approximately as the inverse square of τ for $\tau \approx 0$.

Figure 2 shows $\text{tcr}(q_D\Lambda, 2k_F/k_p)$ plotted against $2k_F/k_p$ for the same $q_D\Lambda$ set (i.e., 2, 4, 6, 12, 18, 300). Note that the range of $2k_F/k_p$ corresponding to negative tcr expands as $q_D\Lambda$ decreases and that even at $q_D\Lambda = 300$ (which yields results undistinguishable from those obtained in the standard Faber-Ziman theory, i.e., $F(q\Lambda) = 1$ in Eqs. (7) and (8)) a significant shift toward larger $2k_F/k_p$ and a broader range of $2k_F/k_p$ for negative tcr is obtained on comparison with the backscattering dominant approximation (ref 8). If some $\text{tcr}_D(q_D\Lambda)$ which is defined in Eq. (21) and is independent of $2k_F/k_p$, is mixed in the range of $2k_F/k_p$ corresponding to negative TCR is increased for $q_D\Lambda < 18$ and decreased for $q_D\Lambda > 18$ with the actual mixture being given by Eq. (21). (For most metallic glasses studied, $q_D\Lambda$ is less than 18.)

Figures 3 through 7 show sets of $R(q_D\Lambda, 2k_F/k_p, \tau)$ vs. τ with $q_D\Lambda$ as a parameter (same set of values as in Figures 1 and 2) for $2k_F/k_p = 0.9, 1.05, 1.15, 1.30, \text{ and } 1.40$, respectively. All the curves in Figure 3, for which $2k_F = 0.9 k_p$, show positive tcr which decreases in magnitude as $q_D\Lambda$ decreases. Small minima which move toward larger τ as $q_D\Lambda$ decreases are seen for $q_D\Lambda < 18$.

Figure 4, for which $2k_F = 1.05 k_p$, corresponds (approximately) to the largest negative tcr. The maximum, which at $q_D\Lambda = 300$ occurs for $\tau_M \approx 0.3$, becomes smaller in magnitude and moves toward lower τ as $q_D\Lambda$ decreases to 12, with $\tau_M \approx 0.15$ for $q_D\Lambda = 12$, while the corresponding minima vary from $\tau_m = 0$ to 0.05. For $q_D\Lambda < 6$ monotonic decreasing curves are exhibited.

Figure 5, for which $2k_F = 1.15 k_p$, is very similar to Figure 4 except that the negative tcr are smaller, etc.

Figure 6, for which $2k_F = 1.30 k_p$, exhibits a change from positive to negative tcr between $q_D\Lambda = 300$ and $q_D\Lambda = 18$. The curves for $q_D\Lambda = 18$ to 6 then show the same trends in τ_m and τ_M as seen in the curves for $q_D\Lambda = 300$ to 12 in Figures 4 and 5. The curve at $q_D\Lambda = 4$ is monotonic with a "knee" at $\tau \approx 0.2$.

Figure 7, for which $2k_F = 1.4 k_p$, is similar to Figure 6 with a transition between positive and negative tcr occurring between $q_D\Lambda = 12$ and 6, with maxima and minima and the expected trends in τ_m and τ_M in the curves for $q_D\Lambda = 6$ and 4, and with monotonic decreasing variation for $q_D\Lambda = 2$.

The effect of mixing in some $R_D(q_D\Lambda, \tau)$ according to the prescription in Eq. (20) is to increase the size of the maxima, to increase τ_M , and to decrease τ_m . Also, if the difference term were dominant (i.e., $K_D \gg K$), then ρ would vary as $c_1(1-c_1)$ rather than as $a(2k_F)$ for an alloy series.

It is also interesting to consider families of ρ vs. τ curves for fixed $q_D\Lambda$. We show detailed results for $q_D\Lambda = 12$ and 6 in Figures 8 and 9. These figures exhibit interesting trends with $2k_F/k_p$. Also for a $q_D\Lambda$ value between 12 and 6 (actually at $q_D\Lambda \approx 10$) monotonic decreasing ρ vs. τ begins to occur for small ranges of $2k_F/k_p$. We see, in particular, that $R(12, 2k_F/k_p, \tau)$ does not decrease monotonically with τ for any $2k_F/k_p$, while there is a small range of $2k_F/k_p$ for which $R(6, 2k_F/k_p, \tau)$ decreases monotonically with τ . As $q_D\Lambda$ decreases the range of $2k_F/k_p$ corresponding to monotonically decreasing ρ vs. τ expands.

For $q_D\Lambda = 12$ the maximum negative TCR occurs for $2k_F/k_p \approx 1.05$. Figure 8(a) shows a selection of curves for $2k_F/k_p > 1.05$ and Figure 8(b) for $2k_F/k_p < 1.05$. Negative tcr curves exhibit maxima (at τ_M) and minima (at τ_m);

positive tcr curves exhibit minima. As $|2k_F/k_p - 1.05|$ increases τ_M increases, $R(12, 2k_F/k_p, \tau_M)$ increases, and τ_m decreases. Eventually, values of $2k_F/k_p$ are reached for which positive tcr occurs and the maxima are gone; however, there are still small minima and τ_m continues to decrease as $|2k_F/k_p - 1.05|$ increases. The largest minimum occurs for $2k_F/k_p \approx 1.00$ and decreases in both directions.

The curves in Figure 9 ($q_D\Lambda = 6$) show all the features seen in Figure 8; in addition, Figure 9 exhibits several monotonically decreasing ρ vs. τ curves for the range of $2k_F/k_p$ near 1.05. For considerably smaller $q_D\Lambda$ the ρ vs. τ curves are monotonically decreasing and vary as $(1-AT^2)$ near $\tau = 0$ for all $2k_F$ in the vicinity of k_p .

Model A2. Substitutional a-Mg_{1-x}Zn_x for $x = 0.225$.

The substitutional a-Mg.775Zn.225 model matrix element (and others for different x) was employed in an earlier study of electrical resistivity in low resistivity amorphous metals (ref 12). A denser set of $2k_F/k_p$, $q_D\Lambda$ values is studied here.

Figure 10 shows tcr vs. $2k_F/k_p$ with $q_D\Lambda$ as parameter. (There is a slight difference between this graph and that shown in Reference 24, since the interpolation is now conducted on a finer grid.) One sees that the curves are very similar to those obtained with constant t-matrix (Figure 2). The principal difference appears to be that the substitutional model (A2) curves are shifted to the left with respect to those computed for the constant t-matrix model (A1). (E.g., for $q_D\Lambda = 300$, Model A2 yields negative tcr for $0.97 \lesssim 2k_F/k_p \lesssim 1.18$ with maximum negative tcr at $2k_F \approx 1.03 k_p$, while model A1 yields negative tcr for $0.99 \lesssim 2k_F/k_p \lesssim 1.22$ with maximum negative tcr at

$2k_F \approx 1.05 k_p$.) The substitutional a-MgZn model also yields slightly larger maximum negative tcr values.

Employing Eq. (18) again to define $R(q_D\Lambda, 2k_F/k_p, \tau)$ with ρ substituted for r on the RHS yields graphs of the form shown in Figures 3 through 9. Except for the shifts in $2k_F/k_p$ discussed in regard to Figure 10 the families of $R(q_D\Lambda, 2k_F/k_p, \tau)$ vs. τ curves produced by model A2 appear essentially the same as the $R(q_D\Lambda, 2k_F/k_p, \tau)$ vs. τ from model A1.

There is another difference which could be discerned in such graphs. For model A2, the $q_D\Lambda$ required for the equivalent curves (i.e., with the shift of $2k_F/k_p$ incorporated) is slightly larger than for model A1. For example, the a-MgZn matrix element results for $q_D\Lambda = 12$, which are shown in Figure 11, look very much like those for the constant t-matrix at $q_D\Lambda = 10$ (not shown); in particular, the A2 model at $q_D\Lambda = 12$ exhibit a range of $2k_F/k_p$ for which monotonic decreasing $R(12, 2k_F/k_p, \tau)$ is obtained. However, for the R scale appropriate for τ between 0 and 1 and the model A1 and A2 ρ vs. τ curves, a strong family resemblance is seen for the same $q_D\Lambda$. (When one examines ρ vs. τ for an R scale appropriate for τ between 0 and 0.3 the correspondence is improved, for example, by comparing curves for model A2 with $2k_F/k_p$ shifted at $q_D\Lambda = 12$ with those of model A1 at $q_D\Lambda = 10$, i.e., shifting $q_D\Lambda$ as well as $2k_F/k_p$ improves the correspondence.)

Other results, based upon the substitutional a-MgZn model for a selection of $2k_F/k_p$ and $q_D\Lambda$ values, were presented in Reference 24. A general conclusion to be drawn is that the R vs. τ curves for model A2 are well approximated by R vs. τ curves for model A1. The K-dependence of the t-matrix for the a-MgZn substitutional model apparently only slightly increases the

phonon ineffectiveness for a given $q_D\Lambda$ and increases the "effective $2k_F/k_p$ " with respect to the constant t-matrix model.

Effective Potential Models

Model B1. a-MgZn adjusted s and p model t-matrix.

This model was discussed for $2k_F \approx 1.1 k_p$ (the appropriate condition in the a-Mg_xZn_{1-x} alloys) in Reference 12. The s and p phase shifts were adjusted to satisfy the Friedel sum rule and to give the observed magnitude of ρ with all other phase shifts zero. The R vs. τ curves for this model are essentially equivalent to those for the a-MgZn substitutional model (or R-type curves deduced for the constant t-matrix case with small $2k_F/k_p$ and $q_D\Lambda$ shifts).

Model B2. Pseudopotential scattering matrix elements.

We noted in Reference 12 that the ρ vs. τ curves for a-MgZn could not be well represented by pseudopotential results. We suggested in that work that the problem with application of diffraction models incorporating pseudopotentials could be in the use of Born approximation. Thus, the work of Young, Meyer, and Kilby (ref 11), in which single site multiple scattering on pseudopotentials was treated to produce sets of scattering phase shifts, seems especially interesting. We have performed calculations based upon the pseudoatom phase shifts of Young, Meyer, and Kilby (ref 11). Figure 12 shows a selection of results computed for the potassium pseudoatom phase shifts for $q_D\Lambda = 12$ and a set of $2k_F/k_p$ values which span the range for negative tcr. All the ρ vs. τ curves exhibit relatively large maxima and $\tau_M > 0.35$. The potassium pseudoatom phase shift results are quite similar to those described in Reference 12 for Born approximation pseudopotential (ref 33) in Mg and Zn

and are representative of our calculations for all the monovalent pseudoatom phase shifts given in Reference 11.

Model B3. Zinc phase shift effective t-matrix.

The Zn phase shifts used in model A2 are used to define this effective t-matrix. Results based upon this t-matrix were given in Reference 24. The magnitude of these phase shifts are comparable to those of the monovalent pseudoatoms (model B2), but the results more closely resemble those of the constant t-matrix except that the magnitudes of the maximum negative tcr's are larger, the range of $2k_F/k_p$ for negative tcr is smaller, and the $q\Lambda$ value required for monotonic decreasing ρ vs. τ is larger.

DISCUSSION

The effect of saturation (as treated in this report) is to reduce the electron-phonon interaction. We have assumed that the longitudinal Pippard function $F(y)$, defined in Eq. (9), gives a reasonable representation of the reduction of the electron-phonon interaction at small $q\Lambda$. Although we have not done extensive studies of the sensitivity of the results to the specific form assumed for $F(y)$, we believe that the results do not depend strongly on how one smoothly interpolates between the small and large $q\Lambda$ limits for which exact expressions are available.

With regard to the suitability of applying the longitudinal Pippard function to general phonons, we might consider the corresponding transverse Pippard (ref 21) function

$$F_t(y) = \frac{\pi}{2} \left[\frac{y^2}{(1+y^2)\tan^{-1}y} - \frac{3}{2y} \right] \quad (9t)$$

Evaluation of $F(y)$ and $F_t(y)$ indicates that the functions differ at most by about six percent for $1 < y < 100$, and by less than eight percent for $0.1 < y < 1$. Thus, for our purposes, $F(y)$ would represent the reduction in electron-phonon interaction of transverse as well as longitudinal phonons.

The semi-classical nature of Pippard's derivation has led to questions pertaining to the validity of using the simple Pippard functions to describe phonon ineffectiveness. Schmid (ref 34) addressed these objections by considering the electron-phonon interaction in finite mean free path metals on a more exact quantum mechanical basis. He succeeded in demonstrating that for s-wave scattering and other reasonable approximations: (i) the longitudinal phonon Greens function appears only in combination with the longitudinal Pippard function, and (ii) the transverse phonon Greens function appears in combination with a form that agrees with the transverse Pippard function at small $q\lambda$. Thus, one may expect that for less restrictive assumptions the Pippard functions approximate the mean free path dependent reduction of the electron-phonon interaction.

Furthermore, it has been demonstrated that ultrasonic attenuation (refs 21,35) and thermal conductivity data (ref 22) are explained by Pippard's theory. Also, the present authors have shown that the degradation of T_c in imperfect strong coupling superconductors (ref 23) and the major resistivity anomalies (i.e., Mooij phenomena) in high resistivity crystalline and amorphous metals (ref 15) are consistent with predictions of a model incorporating phonon ineffectiveness in the manner described here.

The constant t-matrix model (Model A1) yields results which are essentially equivalent to those obtained from the other models studied thus far. The monovalent pseudoatom results (Model B2) can be made to conform with the other model results if fairly large adjustments in $q_D\Lambda$ are allowed. Thus, the model calculations yield $\rho(\tau)$ forms which are essentially determined by structure alone. The effect of the different t-matrix forms is merely to change the $2k_F/k_p$ and $q_D\Lambda$ parameters appropriate to a given $\rho(\tau)$, i.e., drastically different t-matrix forms yield essentially equivalent ρ vs. τ curves.

Some of the effects of employing the integral expression, Eq. (5), rather than the usual "backscattering dominant" expression include: (i) The center of the range of $2k_F/k_p$ yielding negative tcr is shifted to higher values. (ii) The range of values of $2k_F/k_p$ for negative tcr is increased. (iii) Not only are the small maxima in ρ vs. τ predicted in Reference 8 for "backscattering dominant" retained in the averaging process, but in some regions of $2k_F/k_p$ the maxima are actually enhanced by the mixing in of some positive tcr components of S^0 (from smaller K/k_p).

Phonon ineffectiveness effects can be seen in the tcr plots of Figures 2 and 10. The shifts of the positive to negative tcr crossover points produced by going from $q_D\Lambda = 300$ to 18 are comparable in magnitude to those produced by going from "backscattering dominant" to the integral form in the unsaturated theory.

Figures 3 through 7 illustrate phonon ineffectiveness effects for a variety of $2k_F/k_p$. The curves for $q_D\Lambda = 300$ are indistinguishable (on the scales of the figures) from the results of standard theory ($q_D\Lambda = \infty$). Significant deviations from the $q_D\Lambda = 300$ case are apparent already at $q_D\Lambda =$

18. Results (not shown) of other calculations at specific $2k_F/k_p$ indicate that the deviations from Ziman-Faber theory could be observed for $q\Lambda > 30$. Thus, phonon ineffectiveness should be considered in determining the ρ vs. τ behavior of virtually all known amorphous metals!

If the partial (geometric) structure factors and t -matrices are known, the resistivity will be expressed as a linear combination of integrals of the form appearing in the substitutional model. One could parameterize this more general case in terms of a value for $q\Lambda$ and a set of weights and $2k_F/k_p$ values for each partial contribution to ρ . In the simplest case one could keep the constant t -matrix approximation; however, generalizations are obviously possible. A treatment along these lines could lead to observable differences with respect to the substitutional model if the partial structure factor peaks are well separated and $q\Lambda$ is not too small. (It is doubtful, for example, that one could discern differences between an appropriate substitutional model and a calculation based upon partial structure factor peaks separated by ten percent for $q\Lambda < 15$ unless the partial structure factors and/or t -matrices were of dramatically different form.)

If the low energy part of the phonon spectrum is Debye like, then qualitatively different results would not be obtained at low temperatures even if the true phonon density of states and dispersion relations were incorporated into the models. However, it is possible that more realistic spectra might significantly alter results for $\tau \gtrsim 1$. We have not yet explored this question.

The results presented here were obtained on the assumption that $q_D = k_F$. In treating this problem in a general way one might equally well have, for

example, assumed q_D fixed. The value of q_D influences the magnitude of the temperature dependent effects and one could improve the theoretical procedure for a given alloy series by using the best available values for q_D and k_F . The τ -dependent parts of ρ ($R(\tau)$ or tcr) for a fixed q_D and a $q_D = k_F$ calculation would differ by less than ± 20 percent for $1 \leq Z \leq 4$.

Faber-Ziman theory and hence our results yield $\rho(T)$ at constant volume. Thus, in experimental tests of the theory thermal expansions must be considered. One generally assumes that $2k_F/k_p$ is essentially T -independent because x-ray data (refs 36,37) indicate that $k_p^3 \Omega_0$ is constant over extensive temperature ranges (which is consistent with the intuitive notion that only the scale of the structure of an amorphous metal should change during thermal expansion) and the free electron model which implies that $k_F^3 \Omega_0$ is also T -independent. However, volume dependent effects in the scattering matrix elements can be significant. These effects can be incorporated in the diffraction model in a straightforward manner. For example, Hafner (ref 38) found that thermal expansion effects were appreciable in first principles pseudopotential based diffraction model studies of $\rho(T)$ in liquid and amorphous $Mg_{71}Zn_{29}$.

Our primary objective is to describe the implications of the generalized Baym-Faber-Ziman theory (incorporating Pippard-Ziman phonon ineffectiveness) which are determined primarily by the structure of metallic glasses. The results for all the model t -matrices studied do indeed exhibit a strong family resemblance. Even the monovalent pseudoatom results, which are essentially pseudopotential results, are viewed as part of this family, although large adjustments in $q_D \Lambda$ and $2k_F/k_p$ are required to make them conform. We consider

an adjustment of less than 15 percent in $q_D\Lambda$ or less than 3 percent in $2k_F/k_p$ as "small".

To compare computed results with data, one would begin with measured parameters or free electron approximations, for example. The important parameter $q_D\Lambda$ is estimated (free electron model) by:

$$q_D\Lambda = 644(Z/2)^{1/3} (k_F a_H)^{-1} (\rho/\mu\Omega\text{cm})^{-1} \quad (24)$$

where a_H is the Bohr radius. (Note that we relax the $q_D = k_F$ condition to obtain Eq. (24).) The appropriate $q_D\Lambda$ will in general not be one of those shown in the figures. Usually one of the curves given will yield a good approximation. However, one can do better. Linear interpolation for R or τ_{cr} on $\log(q_D\Lambda)$ will yield excellent results for $2 < q_D\Lambda < 18$ and good results for $18 < q_D\Lambda < 300$. For example, to obtain $R(8)$ use

$$R(8) = [\log(12/8)R(6) + \log(8/6)R(12)]/\log(12/6)$$

since curves are given for $q_D\Lambda = 12$ and $q_D\Lambda = 6$. This procedure could be employed to account for the T -dependent changes in $q_D\Lambda$ in a self-consistent manner; however, in practical cases this effect would be only barely perceptible even in extreme cases. (e.g., An extreme case might be a ten percent reduction of ρ from 0°K to room temperature. In such cases a slight upward curvature in ρ vs. T would be generated near room temperature. A single iteration would yield the entire effect within one percent of the change in ρ .)

References 12 and 24 demonstrated that Pippard-Ziman phonon ineffectiveness produced significant effects in low resistivity ($\rho \approx 50 \mu\Omega\text{cm}$) amorphous alloys so we cannot make a clear cut separation into high and low resistivity metals. We shall, somewhat arbitrarily, consider an alloy to have high

resistivity if $q_D\Lambda$ is small enough to produce monotonic decreasing $\rho(\tau)$. For example, for the a-MgZn substitutional model or for the constant t-matrix model, $q_D\Lambda \lesssim 10$ would correspond to high resistivity. Equation (24) shows that k_F and Z as well as ρ play a role in determining "high resistivity" under this definition.

Interesting phenomena (viz., low temperature maxima and/or minima) occur in low resistivity amorphous alloys. Good agreement with the observed size and position of the minima and maxima in $\rho(\tau)$ and reasonable agreement with the tcr can be obtained with either the constant t-matrix or the a-MgZn substitutional model with small adjustments of parameters. A single value of α , consistent with k_F and M , fits the entire ρ vs. τ with a value of the Debye temperature (usually) consistent with tabulated values of the resistivity Debye temperature (denoted as θ_R). This choice of θ might be considered an adjustment to the thermal Debye temperature; θ_R usually differs from the thermal value by less than 30 percent (ref 39).

The predicted tcr vs. $2k_F/k_p$ curve for these models also appears to have the observed form (i.e., negative tcr persists to quite large $2k_F/k_p$ and there is relatively small variation in the magnitude of the tcr for a range of $2k_F/k_p$ near the maximum negative value).

Most glassy metals fall into the high resistivity category and there are many alloy series which exhibit a transition to monotonic decreasing (i.e., high ρ) behavior. There are examples of high resistivity amorphous metals which yield results consistent with the model calculations (ref 40). However, the typical case (ref 17) differs from the theory on critical analysis of the low temperature form of $\rho(\tau)$ and/or the size of the positive deviations from

linearity in $\rho(\tau)$ near $\tau = 1$. This problem is only partially alleviated by accounting for variations of $q_D\Lambda$ as ρ decreases with increasing τ for appropriate α values. Actually, the agreement is reasonably good in many of these high ρ alloys when based upon the standards usually applied to the fitting of resistivity data to diffraction model results.

The origin of the discrepancies in the high resistivity alloys is not known. Some possibilities would include: (i) Realistic phonon spectra. (ii) Appropriate t -matrix forms. (iii) Additional scattering mechanisms related, for example, to two level systems (ref 41). (iv) Saturation effects in the elastic scattering contributions. (v) Incipient localization (ref 42).

CONCLUSIONS

Diffraction model calculations, incorporating the Pippard-Ziman expression to represent phonon ineffectiveness and employing a number of model t -matrices have been performed. Although the results are not very sensitive to the exact form of $F(q\Lambda)$, the Greens function analysis of Schmid (ref 34) and a variety of experimental results controlled by the electron-phonon interaction support the use of this procedure.

The results for low resistivity ($q_D\Lambda > 10$ or $\rho < 100 \mu\Omega\text{cm}$) amorphous metals agree well with the extensive body of data obtained for such systems by Mizutani and coworkers. The alloys studied by these workers are exceptionally well characterized so that direct comparisons are possible. Such features as low temperature minima and maxima in ρ for negative tcr cases and their variations with $q_D\Lambda$ and $2k_F/k_p$ are reproduced. Also, the experimental trends of the tcr with $2k_F/k_p$ are explained; in particular, the shift relative to

backscattering dominant results and the extended range of $2k_F/k_p$ for negative τ are explained. Good agreement with the data is obtained with only small adjustments in $2k_F/k_p$ and/or $q_D\Lambda$ for all the scattering matrix models treated except for the pseudopotential based t-matrix models, which require larger adjustments of the parameters. The larger adjustments in $2k_F/k_p$ and $q_D\Lambda$ that are required to make the pseudopotential based calculations conform suggest that systems which are well-described by pseudopotentials might yield ρ vs. τ curves that appear to be inconsistent with those obtained in the low resistivity alloys studied thus far.

New features are predicted for high resistivity ($q_D\Lambda < 10$ or $\rho > 100 \mu\Omega\text{cm}$) alloys. In particular, monotonic decreasing ρ vs. τ is predicted for $q_D\Lambda$ -dependent ranges of $2k_F/k_p$ and in the short mean free path limit ($q_D\Lambda \lesssim 1$) the low T limiting form $\rho \sim \rho_0(1-AT^2)$ with $A > 0$ is predicted. This type of behavior is well known in high resistivity alloys. However, except for a few cases, the agreement between theory and experiment is only qualitative. In particular, the pronounced sigmoidal character of the measured ρ vs. τ curves is not adequately explained.

REFERENCES

1. T. E. Faber, Liquid Metals (Cambridge University Press, London, 1972).
2. J. M. Ziman, Philos. Mag. 6, 1013 (1961).
3. G. Baym, Phys. Rev. 135, A1691 (1964).
4. P. J. Cote and L. V. Meisel, Phys. Rev. Lett. 39, 102 (1977).
5. L. V. Meisel and P. J. Cote, Phys. Rev. B 16, 2978 (1977).
6. R. Evans, B. L. Gyorffy, N. Szabo, and J. M. Ziman, The Properties of Liquid Metals, edited by S. Takenchi (Wiley, New York, 1973).
7. R. Evans, D. A. Greenwood, and P. Lloyd, Phys. Lett. A 35, 57 (1971).
8. L. V. Meisel and P. J. Cote, Phys. Rev. B 17, 4652 (1978).
9. J. K. Percus, G. J. Yevick, Phys. Rev. 110, 1 (1958). See also J. L. Lebowitz, ibid, 133, A1399 (1964).
10. See, for example, N. W. Ashcroft and J. Leckner, Phys. Rev. 145, 83 (1966).
11. W. H. Young, Axel Meyer, and G. E. Kilby, Phys. Rev. 160, 160 (1967).
12. L. V. Meisel and P. J. Cote, Phys. Rev. B 27, 4617 (1983).
13. U. Mizutani and T. Yoshida, J. Phys. F 12, 2331 (1982), T. Matsuda and U. Mizutani, Solid State Comm. 44, 145 (1982), T. Matsuda and U. Mizutani, J. Phys. F 12, 1877 (1982), T. Matsuda, N. Shiotani, U. Mizutani, J. Phys. F (in press).
14. D. Korn, W. Murer, and G. Zibold, Phys. Lett. 47A, 117 (1972), E. Blasberg, D. Korn, H. Pfeifle, J. Phys. F 9, 1821 (1979).
15. P. J. Cote and L. V. Meisel, Phys. Rev. Lett. 40, 1586 (1978).
16. J. H. Mooij, Phys. Status Solidi A 17, 521 (1973).

17. See, for example, G. Fritsch, J. Willer, A. Wildermuth, and E. Luscher, J. Phys. F 12, 2965 (1982); H. Schroder and W. Felsch, J. Non-Cryst. Sol. 56, 219 (1983); U. Mizutani and T. Matsuda, J. Phys. F 13, 2115 (1983); R. Clarke and S. R. Nagle, Sol. State Comm. 36, 751 (1980).
18. See, for example, Z. Fisk and G. W. Webb, Phys. Rev. Lett. 36, 1084 (1976).
19. N. Morton, B. W. James, G. H. Wostenholm, Cryogenics 18, 131 (1978).
20. J. M. Ziman, Electrons and Phonons, Chap 5 (Clarendon press, Oxford, 1960).
21. A. B. Pippard, Philos. Mag. 46, 1104 (1955), C. Kittel, Quantum Theory of Solids (Wiley, New York, 1964).
22. J. E. Zimmerman, J. Phys. Chem. Solids 11, 299 (1959).
23. L. V. Meisel and P. J. Cote, Phys. Rev. B 19, 4514 (1979).
24. P. J. Cote and L. V. Meisel, Proceedings of the Fifth International Conference on Liquid and Amorphous Metals, UCLA, 1983 (in press); L. V. Meisel and P. J. Cote, *ibid.*
25. P. J. Cote and L. V. Meisel, in Glassy Metals I, edited by H.-J. Guntherodt and H. Beck (Springer, Heidelberg, 1981).
26. U. Mizutani, Prog. Mat. Science (in press).
27. D. G. Naugle, J. Phys. Chem. Solids (in press).
28. See, for example, J. C. Slater and K. H. Johnson, Phys. Rev. 5, 844 (1972).
29. F. C. Herman and S. Skillman, Atomic Structure Calculations (Prentice Hall, Englewood Cliffs, NJ, 1963).
30. T. L. Loucks, Augmented Plane Wave Method (Benjamin, New York, 1967).

31. E. A. Kmetko, Phys. Rev. A 1, 37 (1970).
32. I. Lindau and W. E. Spicer, in Charge Transfer/Electronic Structure of Alloys, edited by L. H. Bennett and R. H. Willens (American Institute of Mining, Metallurgical, and Petroleum Engineers, 1974).
33. W. A. Harrison, Pseudopotentials in the Theory of Metals (Benjamin, New York, 1966).
34. A. Schmid, Z. Physik 259, 421 (1973).
35. W. A. Fate, Ph.D. Thesis, Rensselaer Polytechnic Institute, 1967 (unpublished).
36. P. J. Cote, G. P. Capsimalis, and L. V. Meisel, Phys. Rev. B 16, 4651 (1977).
37. Y. Waseda and T. Masumoto, Sci. Rep. Res. Inst. Tohoku Univ 27A, (1978).
38. J. Hafner, J. Non-Cryst. Solids (in press).
39. G. T. Meaden, Electrical Resistance in Metals (Plenum Press, New York, 1965).
40. L. V. Meisel and P. J. Cote, Phys. Rev. B 15, 2970 (1977).
41. See, for example, R. Harris, J. Strom-Olsen, and M. Zuckerman, Phys. Rev. Lett. 35, 676 (1975).
42. See, for example, M. Jonson and S. M. Girvin, Phys. Rev. Lett. 43, 1447 (1979); Y. Imry, Phys. Rev. Lett. 44, 469 (1980).

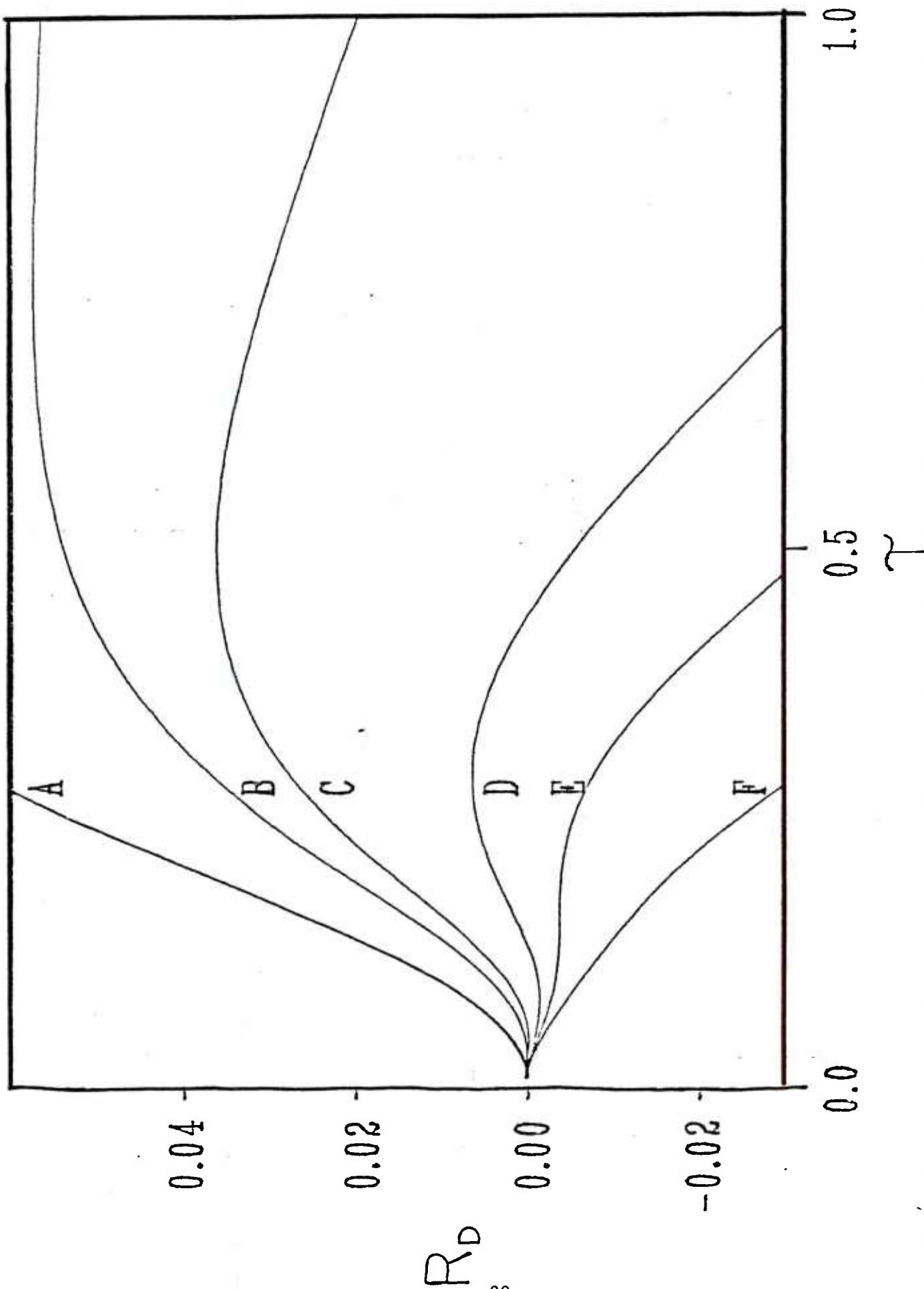


Figure 1. Normalized resistivity difference (Eq. (19)) for the $|t_1 - t_2|^2$ term in Eq. (12b) versus normalized temperature (Eq. (16)) for the constant t-matrix substitutional model. The curves in Figures 1 through 7 parameterized A, B, C, D, E, and F designate results for $q\mu\Lambda = 300, 18, 12, 6, 4,$ and $2,$ respectively.

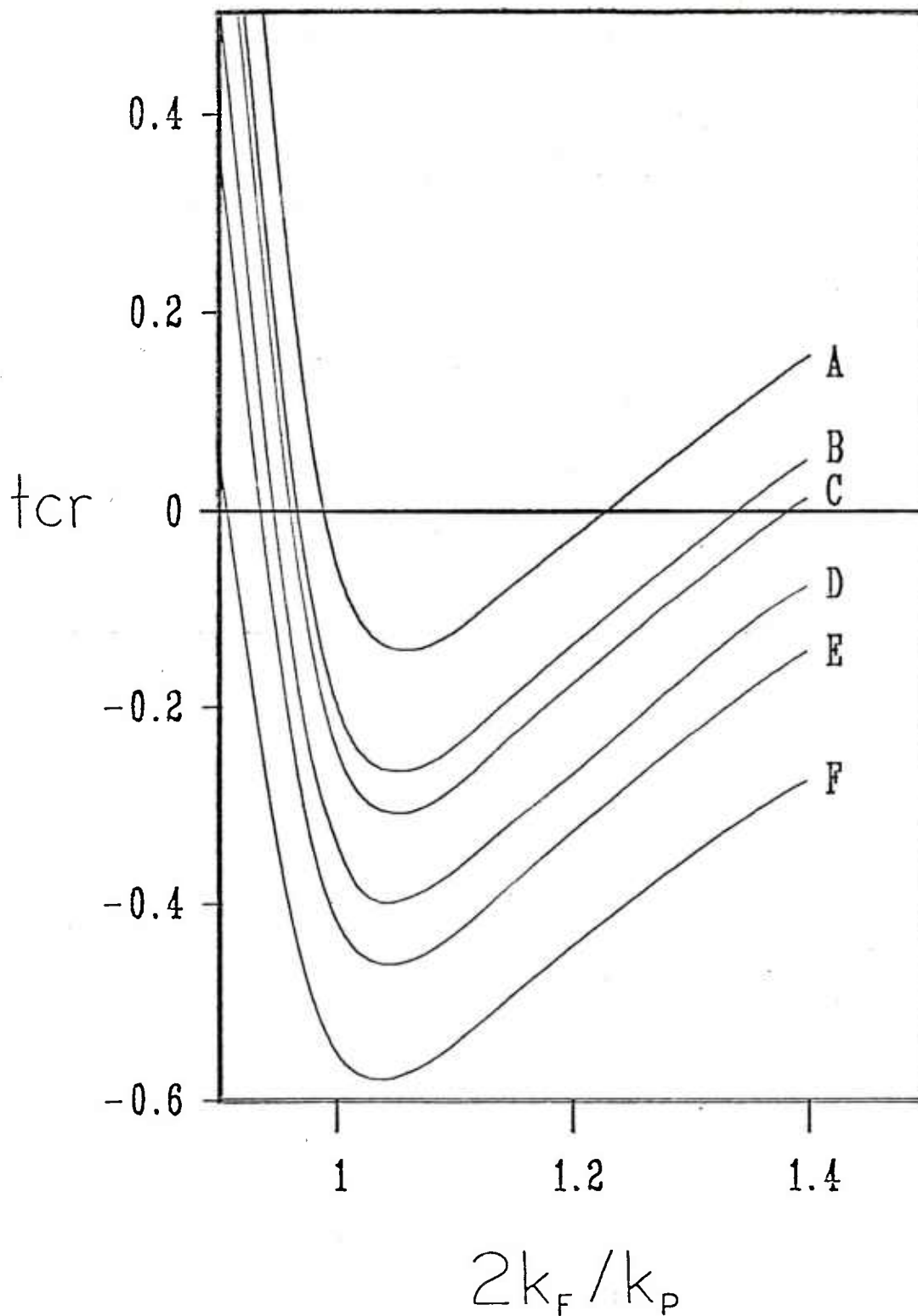


Figure 2. Normalized temperature coefficient of resistivity (Eq. (17) for the averaged t-matrix term (i.e., the $|c_1 t_1 + c_2 t_2|^2$ term) in Eq. (12b) versus $2k_F/k_p$ for the constant t-matrix substitutional model. (Parameters as in Figure 1.)

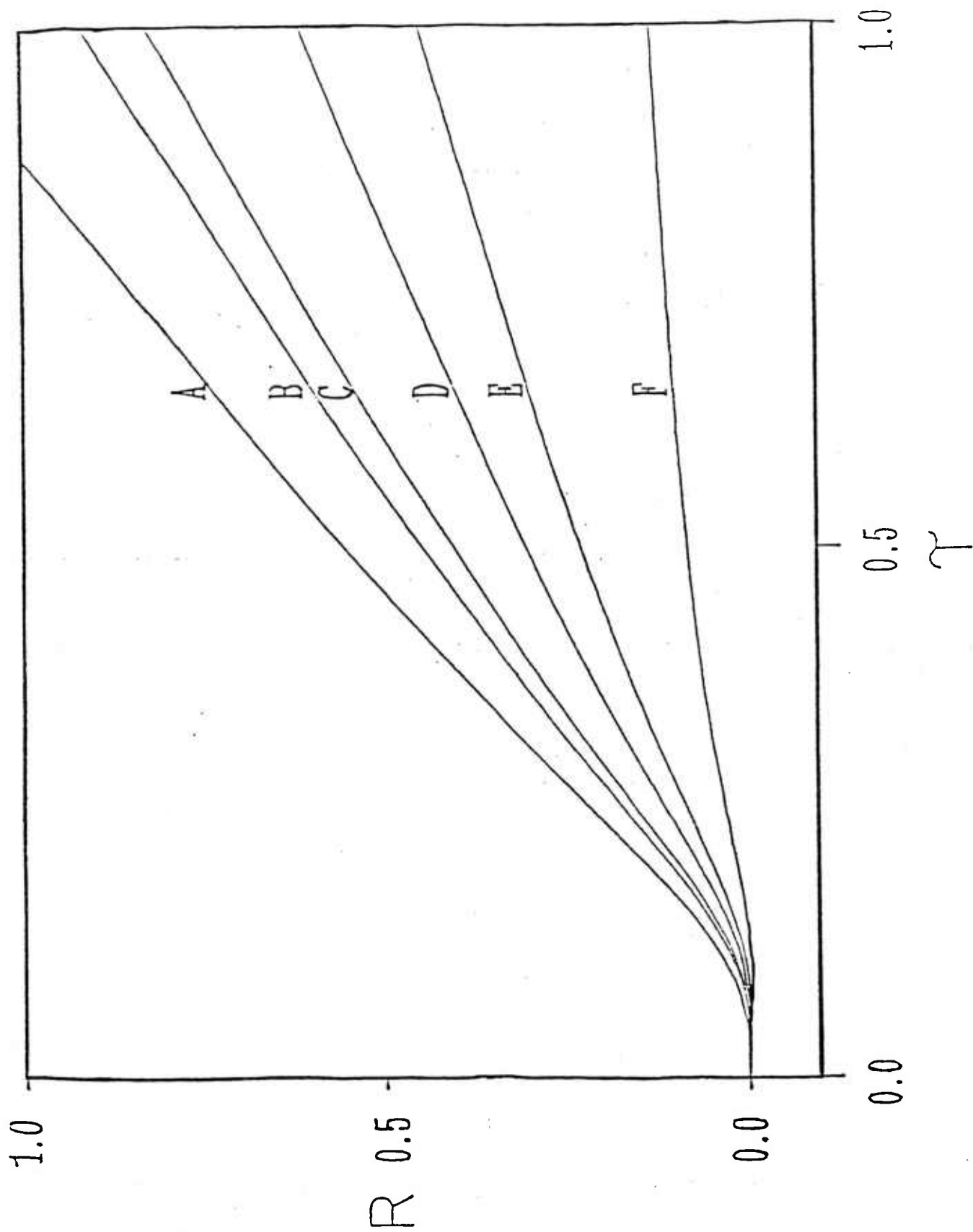


Figure 3. Normalized resistivity difference (Eq. (18)) for the averaged t-matrix term in Eq. (12b) versus normalized temperature (Eq. (16)) for the constant t-matrix substitutional model for $2k_F = 0.9 k_p$. (Parameters as in Figure 1.)

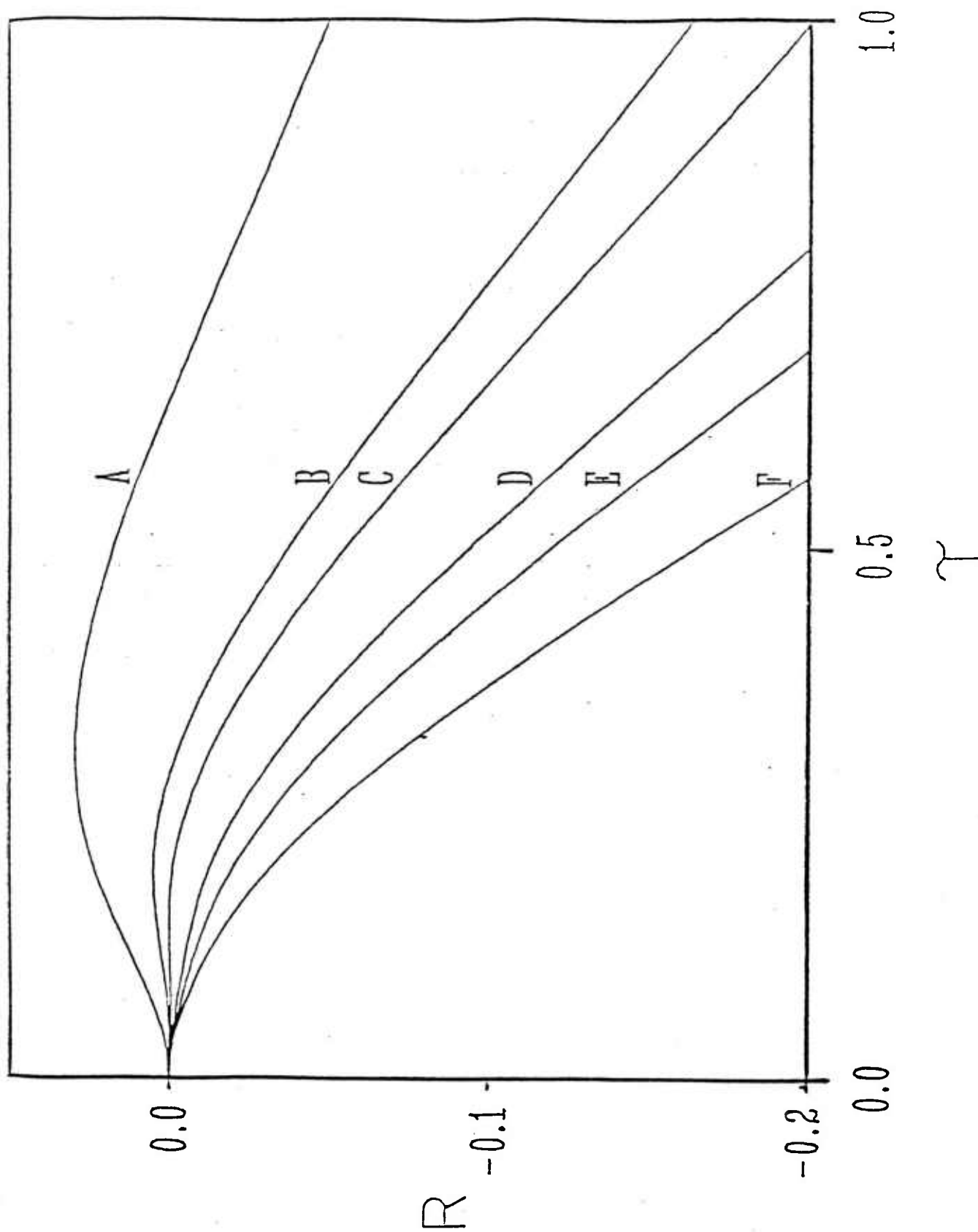


Figure 4a. Normalized resistivity difference versus normalized temperature as in Figure 3 for $2k_F = 1.05$.

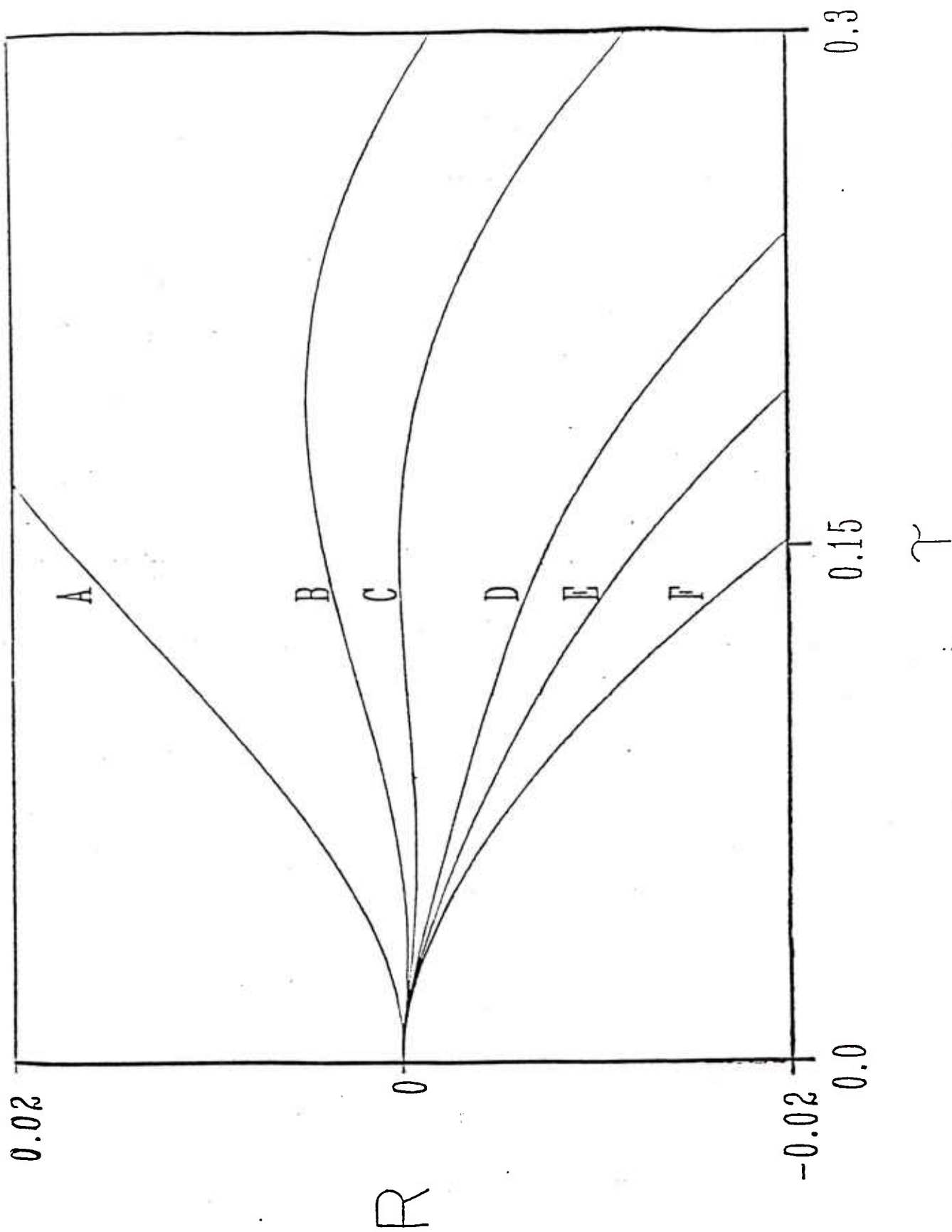


Figure 4b. Normalized resistivity difference versus normalized temperature as in Figure 3 for $2k_F = 1.05 k_p$.

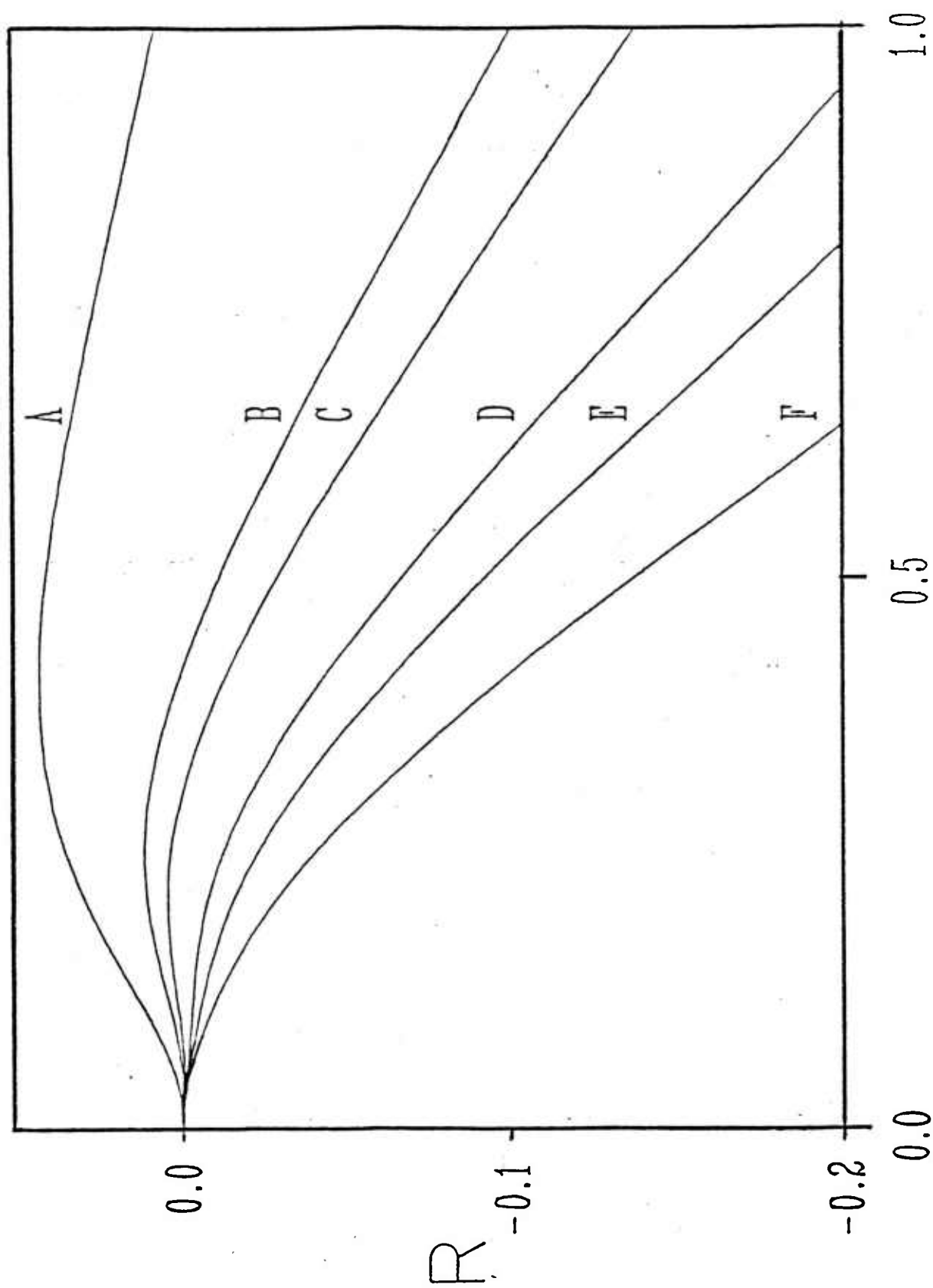


Figure 5a. Normalized resistivity difference versus normalized temperature as in Figure 3 for $2k_F = 1.15 k_p$.

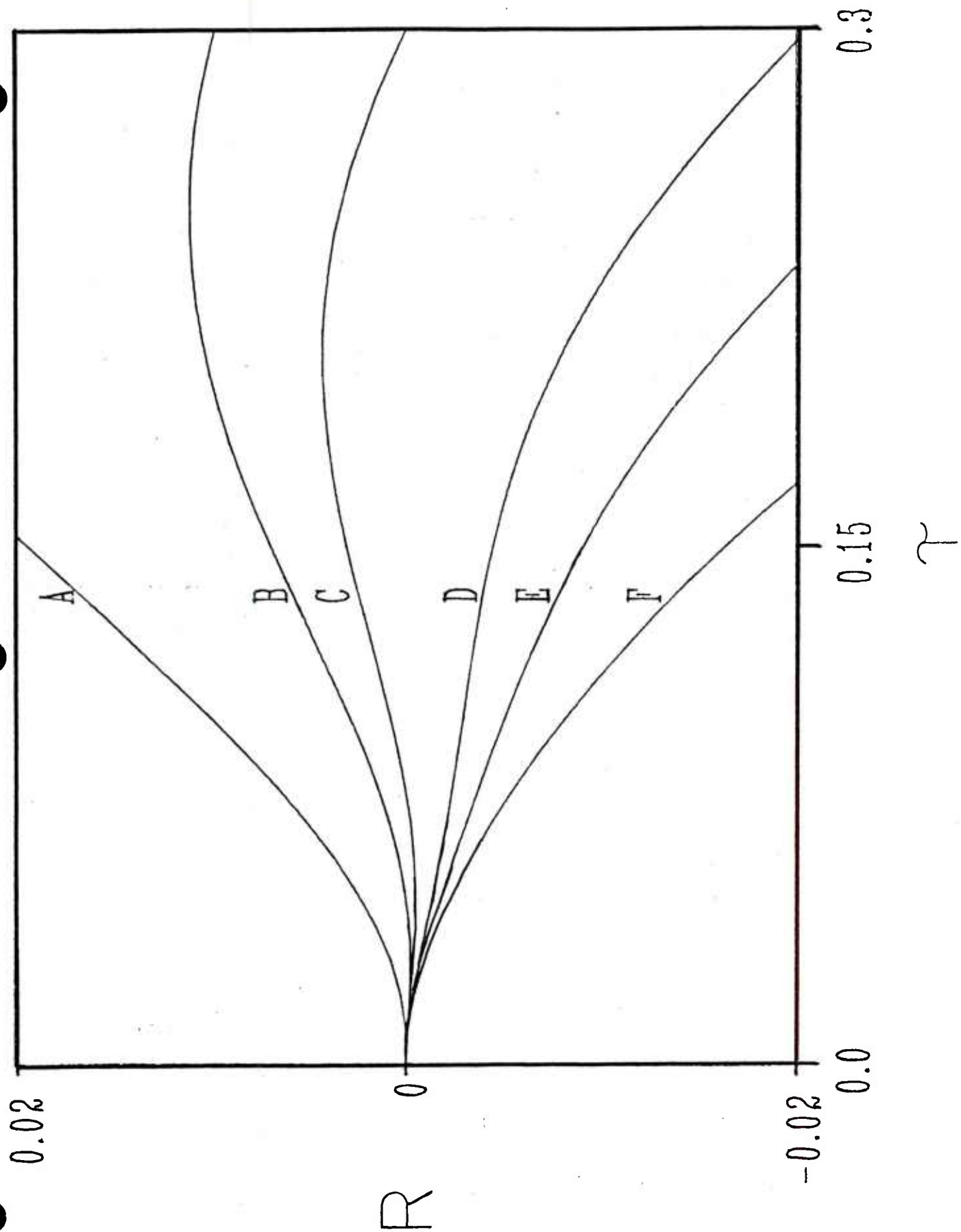


Figure 5b. Normalized resistivity difference versus normalized temperature as in Figure 3 for $2k_F = 1.15 k_p$.

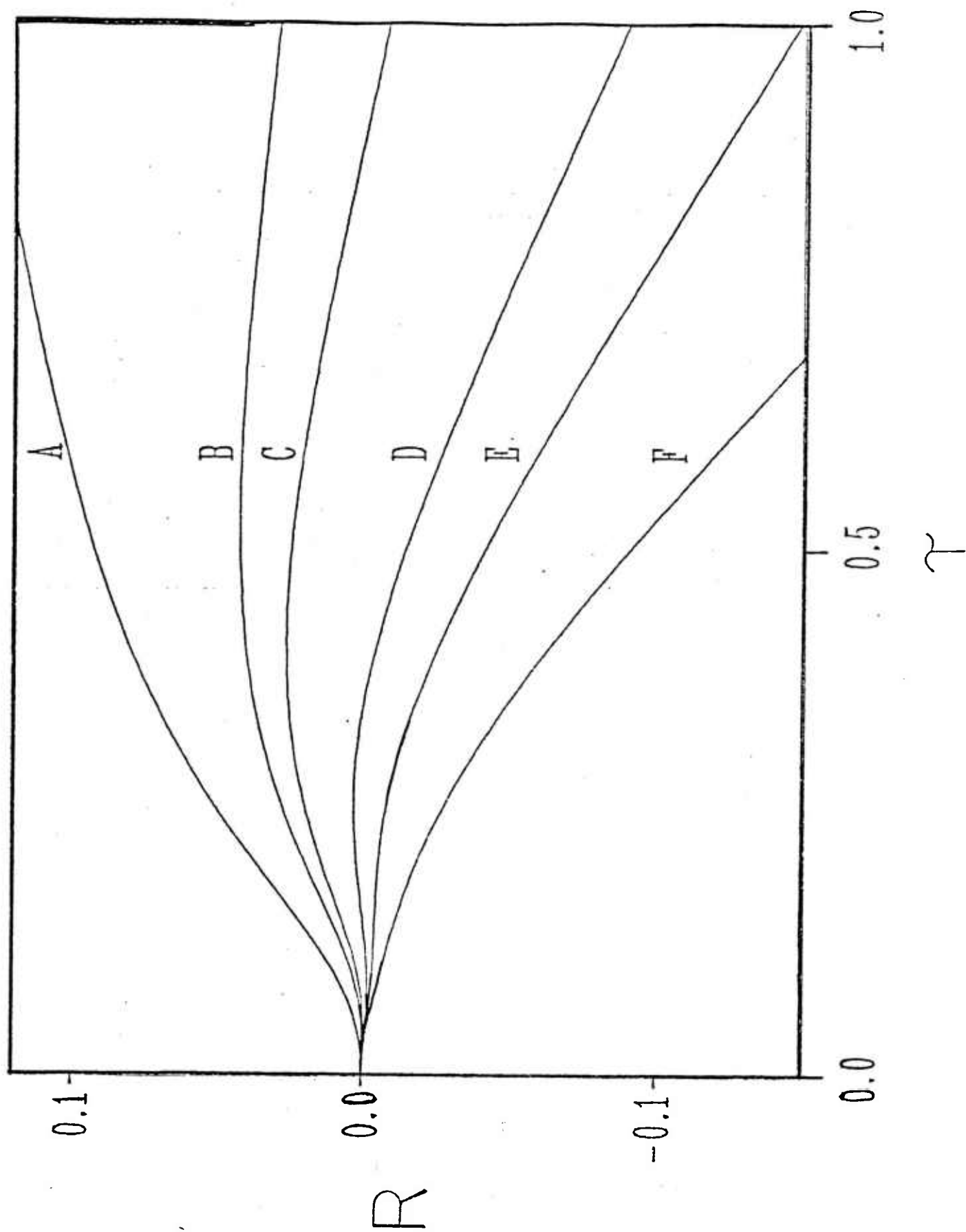


Figure 6a. Normalized resistivity difference versus normalized temperature as in Figure 3 for $2k_F = 1.30 \text{ k_F}$.

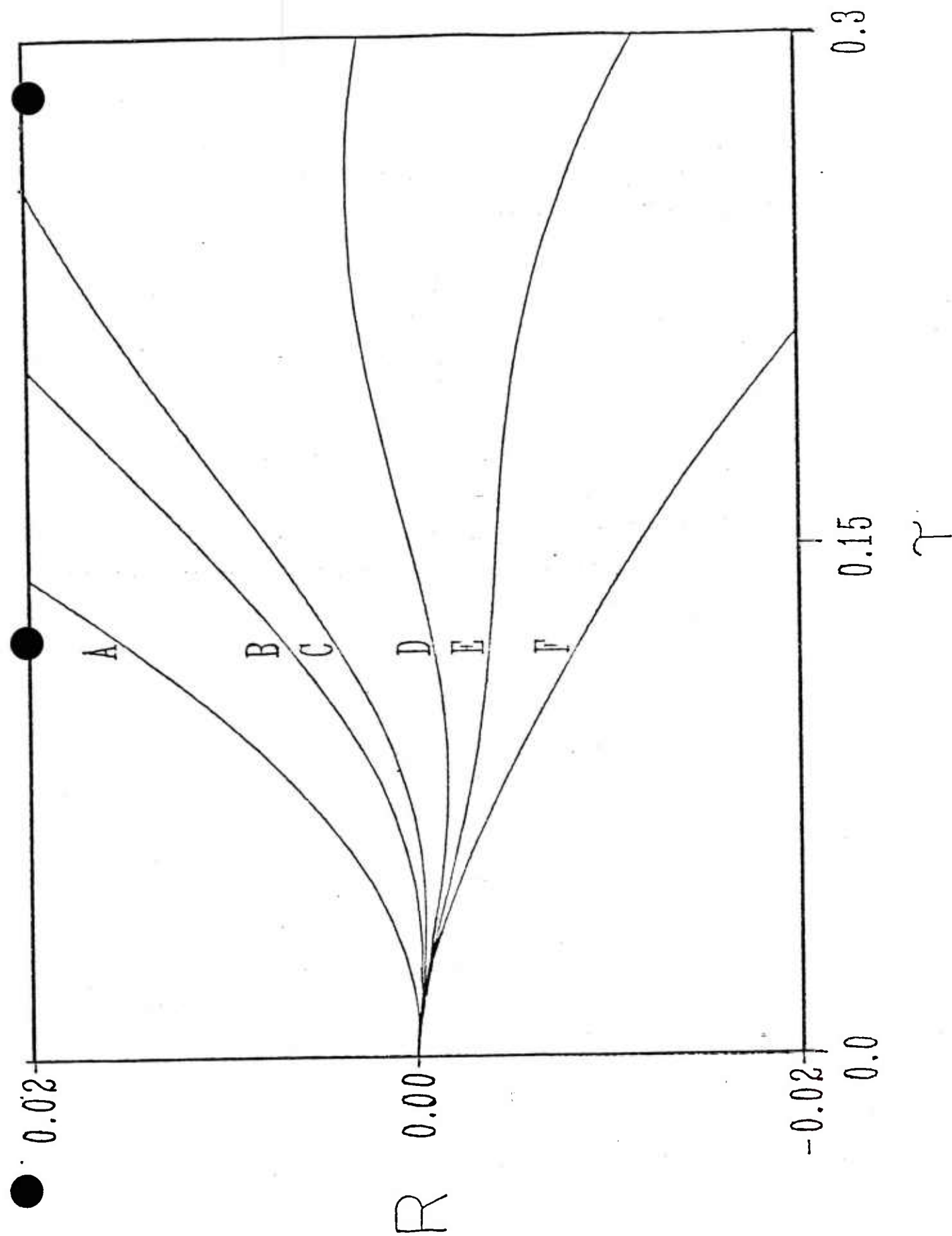


Figure 6b. Normalized resistivity difference versus normalized temperatures as in Figure 3 for $2k_F = 1.30 k_p$.

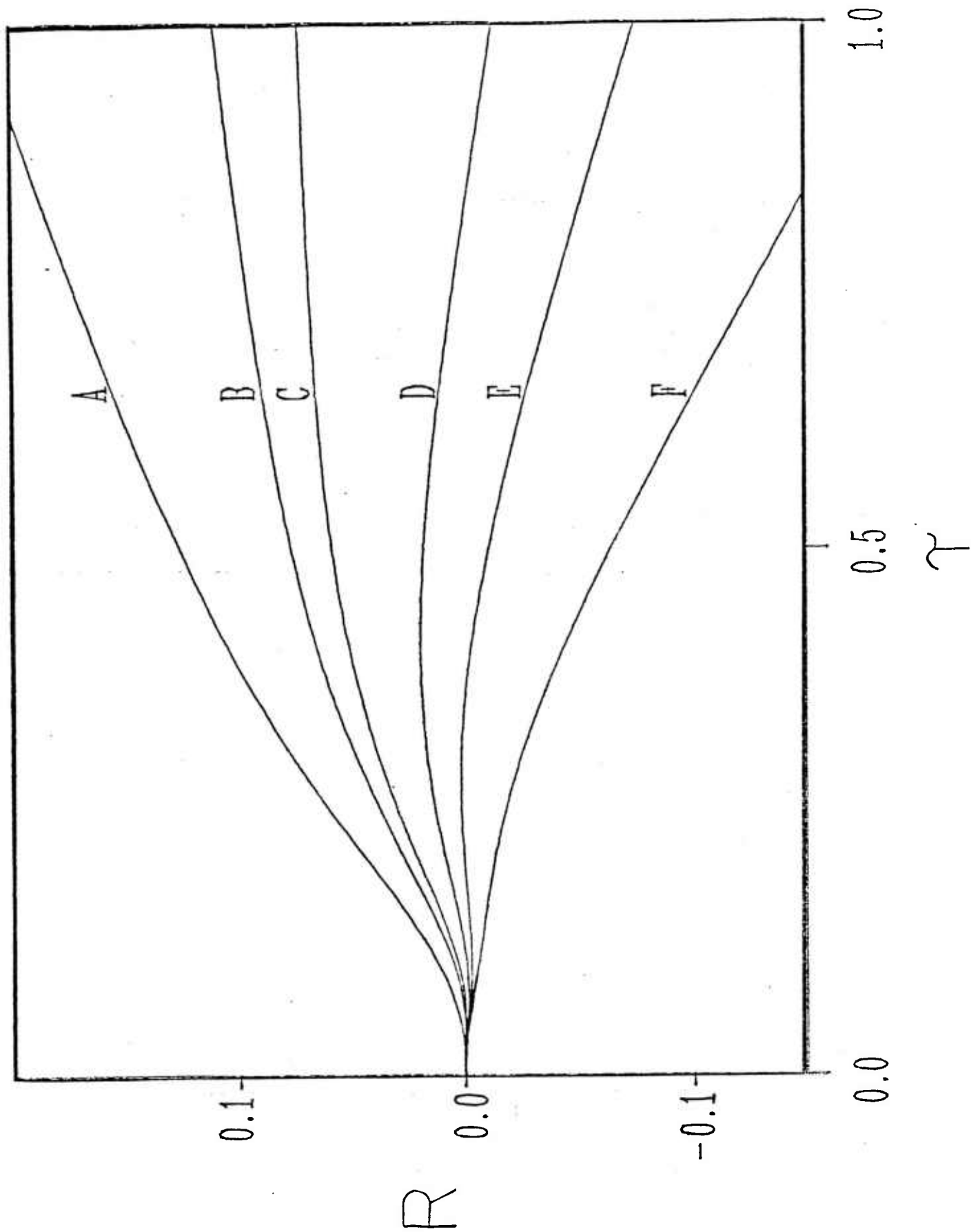


Figure 7a. Normalized resistivity difference versus normalized temperature as in Figure 3 for $2k_F = 1.40 k_p$.

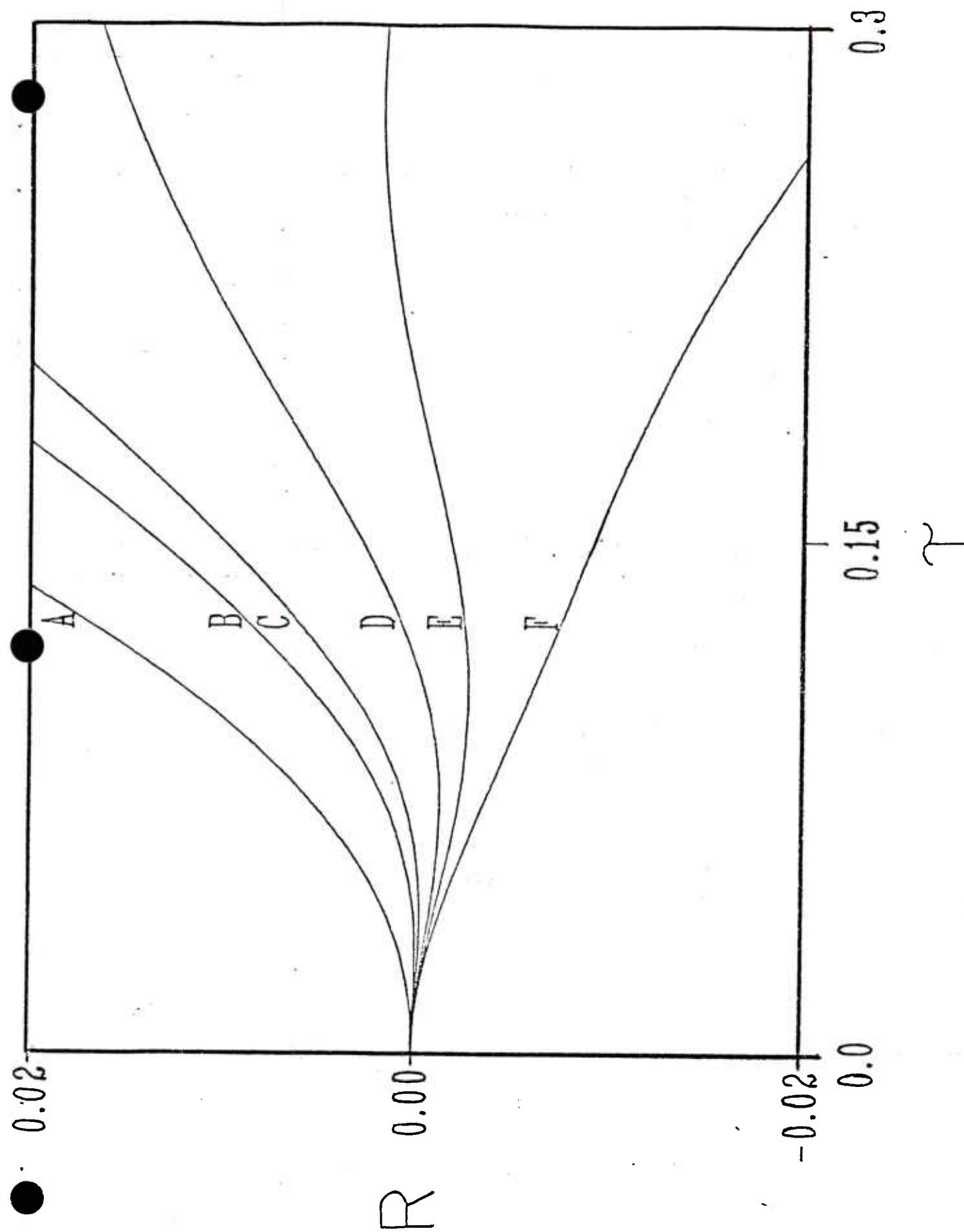


Figure 7b. Normalized resistivity difference versus normalized temperature as in Figure 3 for $2k_F = 1.40 k_p$.

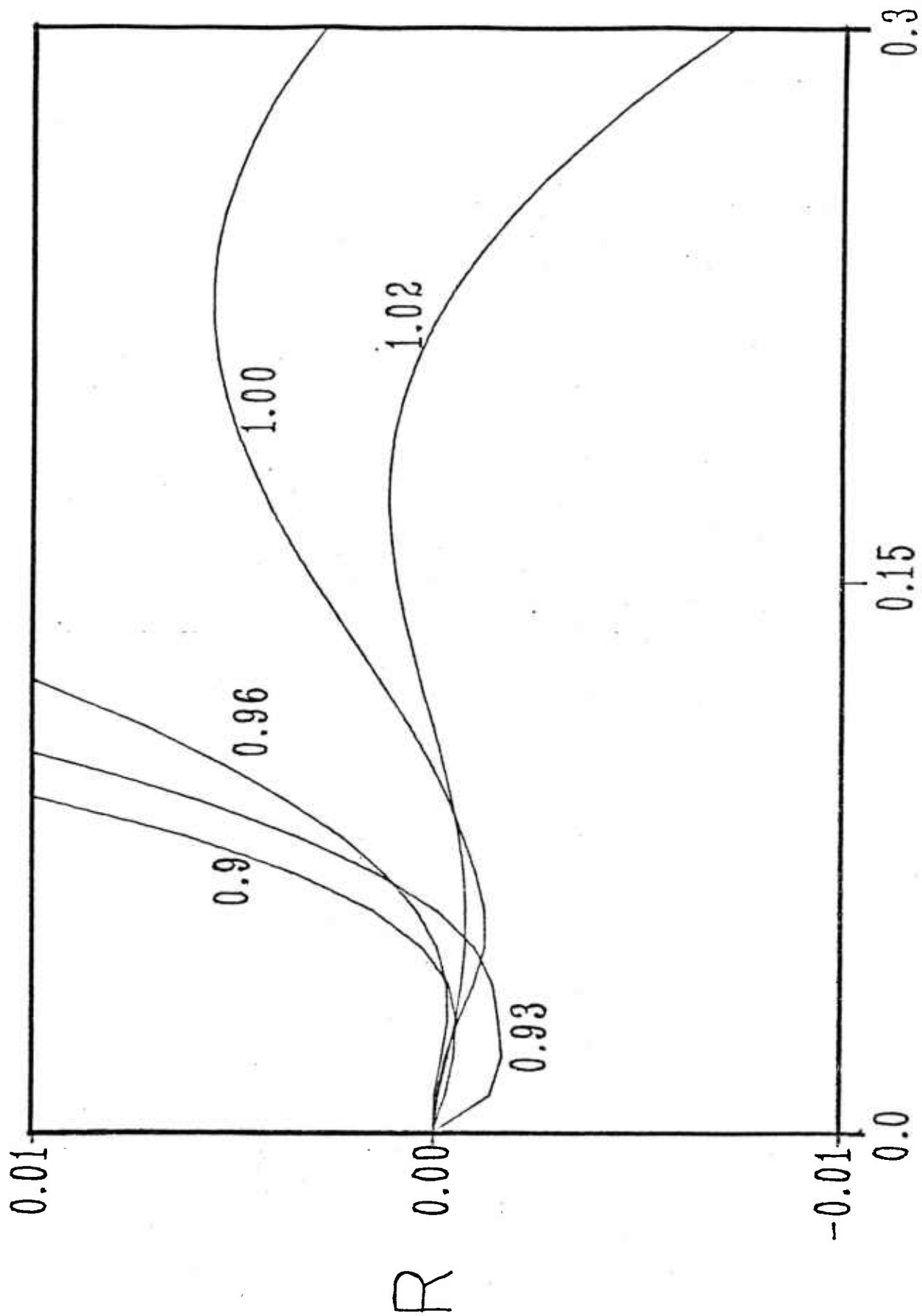


Figure 8a. Normalized resistivity difference versus normalized temperature as in Figure 3 for $qp\Lambda = 12$. The parameters are $2k_f/k_p$ values. Parts (a) and (b) are from the left and right of $2k_f/k_p$ corresponding to the largest negative t .

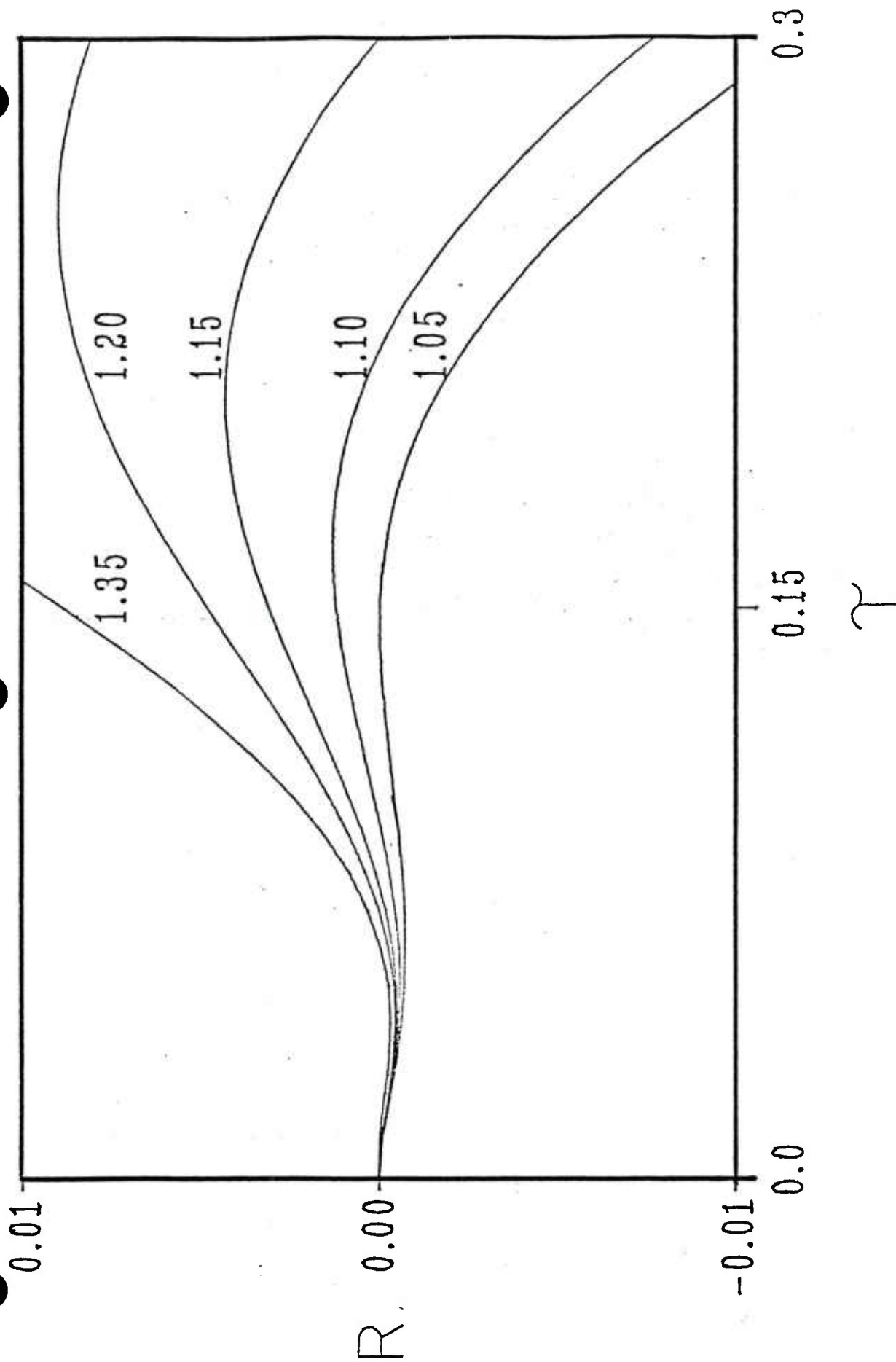


Figure 8b. Normalized resistivity difference versus normalized temperature as in Figure 3 for $q\mu\Lambda = 12$. The parameters are $2k_F/k_p$ values. Parts (a) and (b) are from the left and right of $2k_F/k_p$ corresponding to the largest negative t_{cr} .

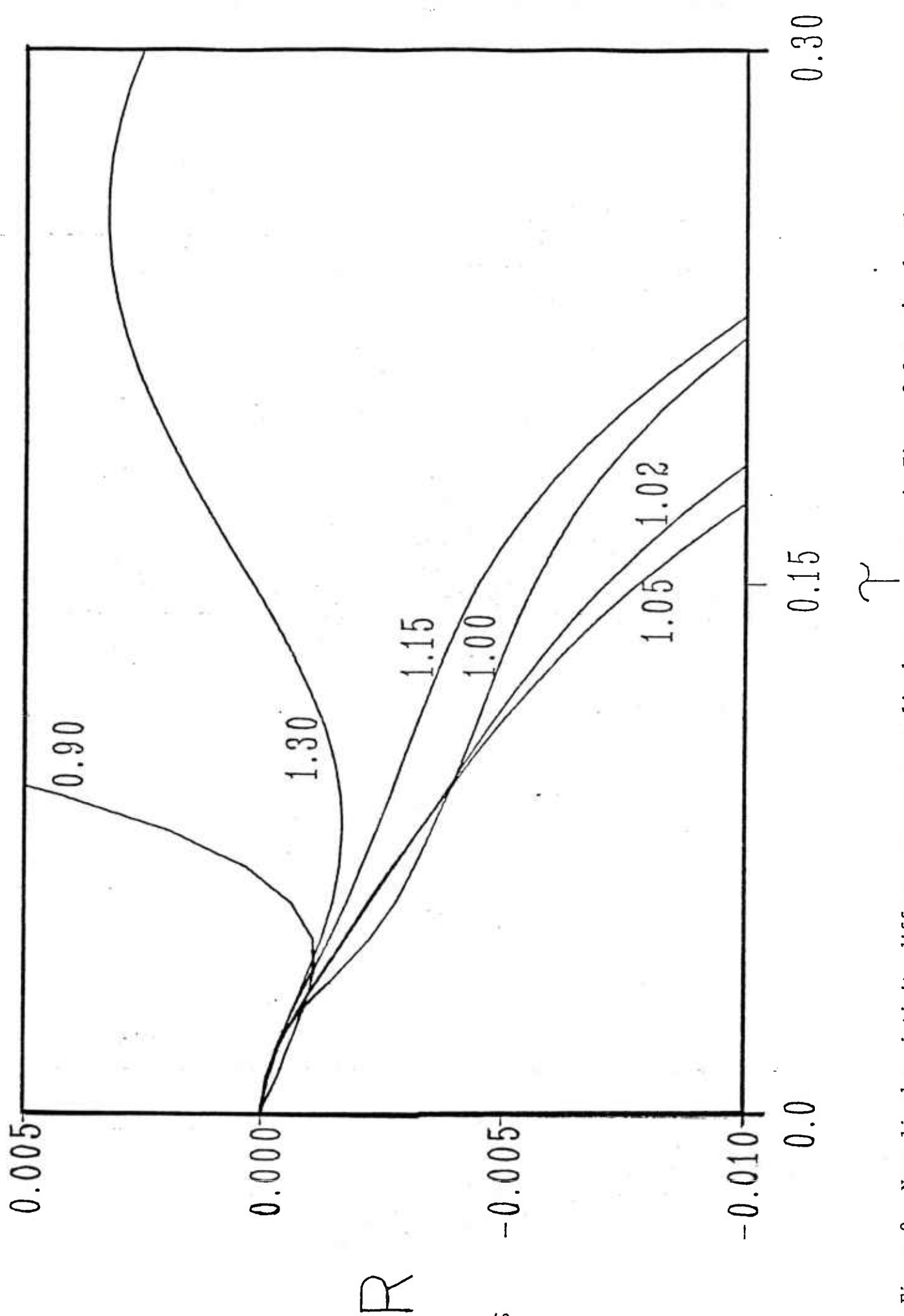


Figure 9. Normalized resistivity difference versus normalized temperature as in Figure 3 for $q_D\Lambda = 6$. The parameters are $2k_F/k_p$ values.

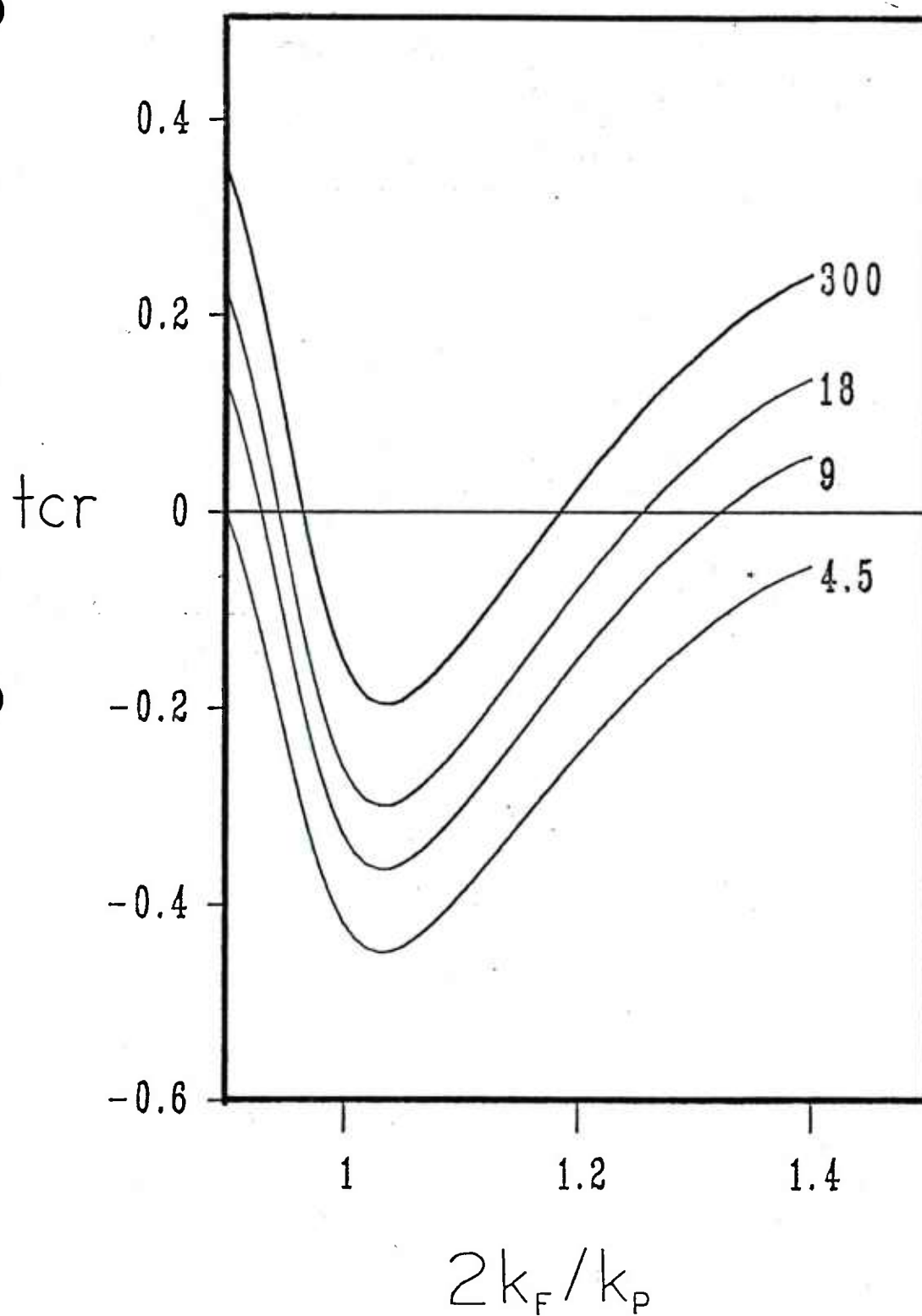


Figure 10. Normalized temperature coefficient of resistivity (Eq. (17)) versus $2k_F/k_P$ for the α - Mg_7Zn_3 substitutional model. The parameters are $q_D\lambda$ values.

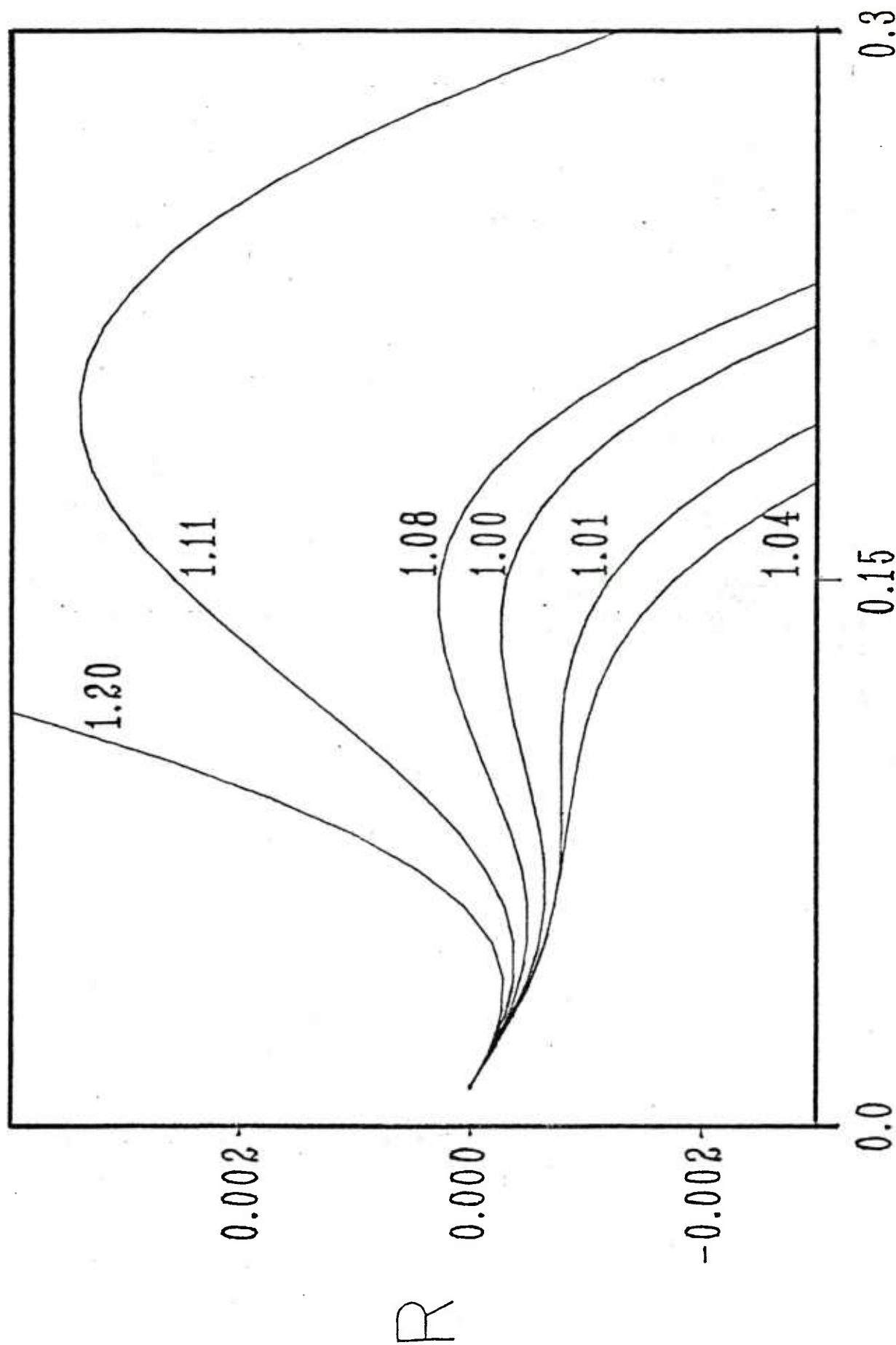


Figure 11. Normalized resistivity difference (ρ substituted for τ in Eq. (18) versus normalized temperature for the a-Mg₇Zn₃ substitutional model with $q_D\Lambda = 12$. The parameters are $2k_F/k_p$ values. (N.b. \bullet Normalization is with respect to ρ at $\tau = 0$ rather than $\tau = 0$ in this and the next figure, \bullet .)

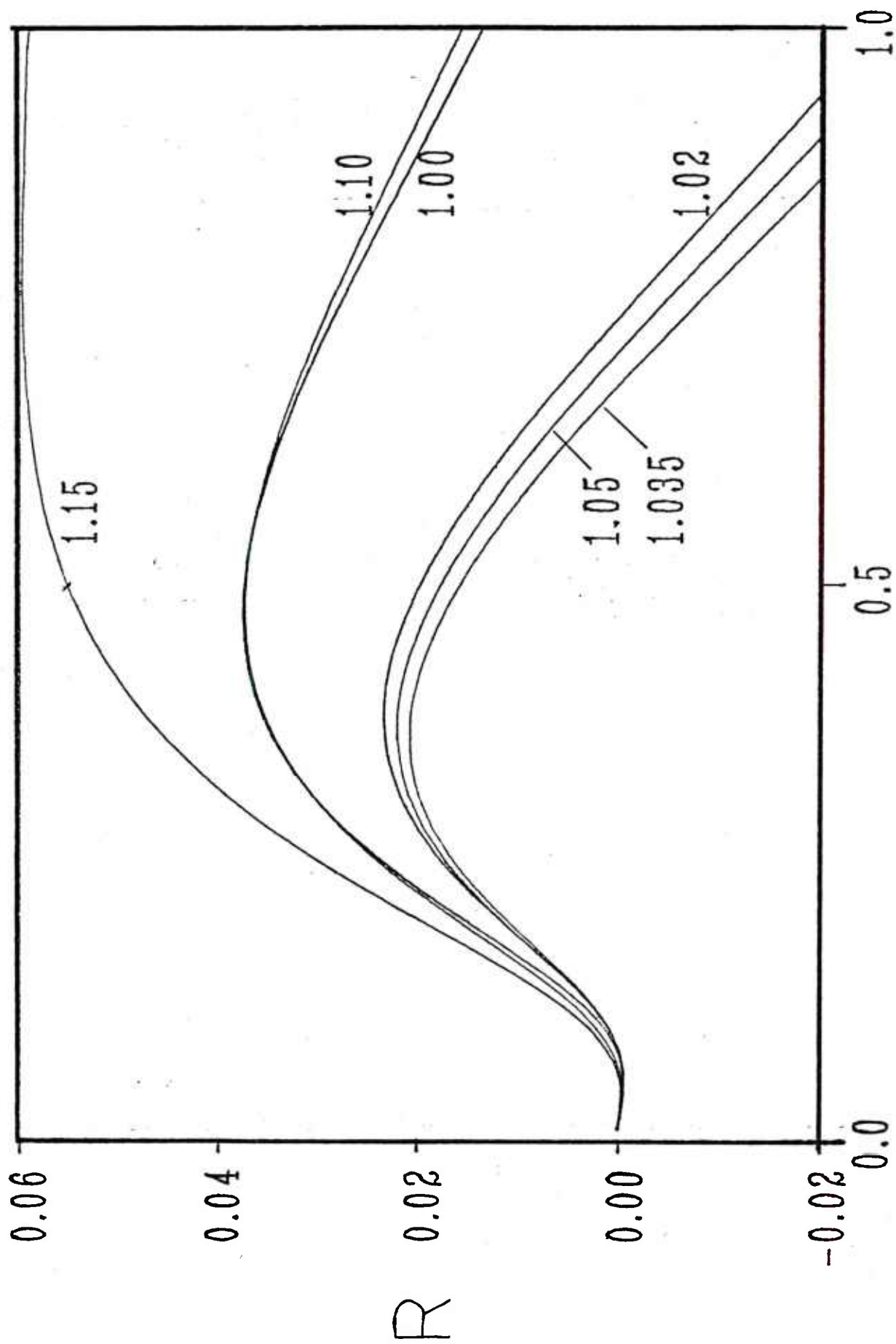


Figure 12. Normalized resistivity difference versus normalized temperature for the potassium pseudoatom effective potential model with $q_D \Lambda = 12$. The parameters are $2k_F/k_p$ values.

TECHNICAL REPORT INTERNAL DISTRIBUTION LIST

	<u>NO. OF COPIES</u>
CHIEF, DEVELOPMENT ENGINEERING BRANCH	
ATTN: SMCAR-LCB-D	1
-DA	1
-DP	1
-DR	1
-DS (SYSTEMS)	1
-DS (ICAS GROUP)	1
-DC	1
CHIEF, ENGINEERING SUPPORT BRANCH	
ATTN: SMCAR-LCB-S	1
-SE	1
CHIEF, RESEARCH BRANCH	
ATTN: SMCAR-LCB-R	2
-R (ELLEN FOGARTY)	1
-RA	1
-RM	2
-RP	1
-RT	1
TECHNICAL LIBRARY	5
ATTN: SMCAR-LCB-TL	
TECHNICAL PUBLICATIONS & EDITING UNIT	2
ATTN: SMCAR-LCB-TL	
DIRECTOR, OPERATIONS DIRECTORATE	1
DIRECTOR, PROCUREMENT DIRECTORATE	1
DIRECTOR, PRODUCT ASSURANCE DIRECTORATE	1

NOTE: PLEASE NOTIFY DIRECTOR, BENET WEAPONS LABORATORY, ATTN: SMCAR-LCB-TL,
OF ANY ADDRESS CHANGES.

TECHNICAL REPORT EXTERNAL DISTRIBUTION LIST

	<u>NO. OF COPIES</u>		<u>NO. OF COPIES</u>
ASST SEC OF THE ARMY RESEARCH & DEVELOPMENT ATTN: DEP FOR SCI & TECH THE PENTAGON WASHINGTON, D.C. 20315	1	COMMANDER US ARMY AMCCOM ATTN: SMCAR-ESP-L ROCK ISLAND, IL 61299	1
COMMANDER DEFENSE TECHNICAL INFO CENTER ATTN: DTIC-DDA CAMERON STATION ALEXANDRIA, VA 22314	12	COMMANDER ROCK ISLAND ARSENAL ATTN: SMCRI-ENM (MAT SCI DIV) ROCK ISLAND, IL 61299	1
COMMANDER US ARMY MAT DEV & READ COMD ATTN: DRCDE-SG 5001 EISENHOWER AVE ALEXANDRIA, VA 22333	1	DIRECTOR US ARMY INDUSTRIAL BASE ENG ACTV ATTN: DRXIB-M ROCK ISLAND, IL 61299	1
COMMANDER ARMAMENT RES & DEV CTR US ARMY AMCCOM ATTN: SMCAR-LC SMCAR-LCE SMCAR-LCM (BLDG 321) SMCAR-LCS SMCAR-LCU SMCAR-LCW SMCAR-SCM-O (PLASTICS TECH EVAL CTR, BLDG. 351N) SMCAR-TSS (STINFO) DOVER, NJ 07801	1 1 1 1 1 1 1 2	COMMANDER US ARMY TANK-AUTMV R&D COMD ATTN: TECH LIB - DRSTA-TSL WARREN, MI 48090 COMMANDER US ARMY TANK-AUTMV COMD ATTN: DRSTA-RC WARREN, MI 48090 COMMANDER US MILITARY ACADEMY ATTN: CHMN, MECH ENGR DEPT WEST POINT, NY 10996 US ARMY MISSILE COMD REDSTONE SCIENTIFIC INFO CTR ATTN: DOCUMENTS SECT, BLDG. 4484 REDSTONE ARSENAL, AL 35898	1 1 1 1 1 1 2
DIRECTOR BALLISTICS RESEARCH LABORATORY ATTN: AMXBR-TSB-S (STINFO) ABERDEEN PROVING GROUND, MD 21005	1	COMMANDER US ARMY FGN SCIENCE & TECH CTR ATTN: DRXST-SD 220 7TH STREET, N.E. CHARLOTTESVILLE, VA 22901	1
MATERIEL SYSTEMS ANALYSIS ACTV ATTN: DRXSY-MP ABERDEEN PROVING GROUND, MD 21005	1		

NOTE: PLEASE NOTIFY COMMANDER, ARMAMENT RESEARCH AND DEVELOPMENT CENTER,
US ARMY AMCCOM, ATTN: BENET WEAPONS LABORATORY, SMCAR-LCB-TL,
WATERVLIET, NY 12189, OF ANY ADDRESS CHANGES.

TECHNICAL REPORT EXTERNAL DISTRIBUTION LIST (CONT'D)

	<u>NO. OF COPIES</u>		<u>NO. OF COPIES</u>
COMMANDER		DIRECTOR	
US ARMY MATERIALS & MECHANICS		US NAVAL RESEARCH LAB	
RESEARCH CENTER	2	ATTN: DIR, MECH DIV	1
ATTN: TECH LIB - DRXMR-PL		CODE 26-27, (DOC LIB)	1
WATERTOWN, MA 01272		WASHINGTON, D.C. 20375	
COMMANDER		COMMANDER	
US ARMY RESEARCH OFFICE		AIR FORCE ARMAMENT LABORATORY	
ATTN: CHIEF, IPO	1	ATTN: AFATL/DLJ	1
P.O. BOX 12211		AFATL/DLJG	1
RESEARCH TRIANGLE PARK, NC 27709		EGLIN AFB, FL 32542	
COMMANDER		METALS & CERAMICS INFO CTR	
US ARMY HARRY DIAMOND LAB		BATTELLE COLUMBUS LAB	1
ATTN: TECH LIB	1	505 KING AVENUE	
2800 POWDER MILL ROAD		COLUMBUS, OH 43201	
ADELPHIA, MD 20783			
COMMANDER			
NAVAL SURFACE WEAPONS CTR			
ATTN: TECHNICAL LIBRARY	1		
CODE X212			
DAHLGREN, VA 22448			

NOTE: PLEASE NOTIFY COMMANDER, ARMAMENT RESEARCH AND DEVELOPMENT CENTER,
US ARMY AMCCOM, ATTN: BENET WEAPONS LABORATORY, SMCAR-LCB-TL,
WATERVLIET, NY 12189, OF ANY ADDRESS CHANGES.